7-Tesla evidence for columnar and rostral–caudal organization of the human periaqueductal grey response in the absence of threat: a working memory study.

Alexandra K. Fischbach[1], Ajay B. Satpute[1, 4], Karen S. Quigley[1, 7], Philip A. Kragel[2, 3], Marta Bianciardi[4], Lawrence L. Wald[4], Tor D. Wager[6], Lisa Feldman Barrett[1, 4, 5*], Jordan E. Theriault[1,4*]

*Shared senior authorship

Affiliations:

[1]Department of Psychology, Northeastern University, Boston, MA 02115 USA

[2]Institute of Cognitive Science, University of Colorado Boulder, Boulder, CO 80309 USA

[3]Department of Psychology, Emory University, Atlanta, GA 30322 USA

[4]Department of Psychiatry, [5]Athinoula A. Martinos Center for Biomedical Imaging, Massachusetts General Hospital and Harvard Medical School, Boston, MA 02115 USA

[6]Department of Psychological and Brain Sciences, Dartmouth College, Hanover, NH 03755 USA.

[7]Center for Healthcare Organization and Implementation Research (CHOIR), Bedford VA Healthcare System, Bedford, MA 01730

Abstract

The periaqueductal grey (PAG) is a small midbrain structure that surrounds the cerebral aqueduct, regulates brain–body communication, and is often studied for its role in "fight-or-flight" defense responses. We used ultra-high field 7-Tesla fMRI to resolve the PAG in humans and distinguish it from the cerebral aqueduct, examining its *in vivo* function in humans during a working memory task (N = 87)—i.e., a setting that required physiological mobilization, but no "threat". During both low and moderate task-elicited cognitive demand, we observed BOLD signal intensity increases in bilateral ventrolateral PAG (vlPAG), consistent with the columnar organization of PAG function identified in non-human animal research. Changes in physiological activity during the task (phasic skin conductance response (SCR) amplitudes, cardiac interbeat interval, respiratory rate) were correlated with PAG BOLD estimates across subjects, and showed some evidence of spatial organization within the PAG, but no spatial organization overlapping with the task-elicited increase in bilateral vlPAG. These findings suggest that the PAG coordinates and regulates bodily activity, even in the absence of threat.

Introduction

The periaqueductal grey (PAG) has historically been identified as a key brain structure mediating the "fight-or-flight" response (e.g., Skultety, 1963; for review, see Bandler, 1988). Human and non-human animal evidence for PAG function has generally been consistent with this interpretation. For example, in cats, stimulating the PAG elicits motor behaviors and physiological responses, ranging from immobility, pupil dilation, vocalization (e.g., hissing or howling), alert positions (Bandler & Carrive, 1988), running and jumping (S. P. Zhang et al., 1990), and hypertension and tachycardia (Abrahams et al., 1960). Deep-brain stimulation of the human PAG elicits feelings of fear, impending death (Nashold et al., 1969), and the need to escape (Amano et al., 1978). Furthermore, functional neuroimaging (fMRI) studies have observed PAG blood-oxygen level-dependent (BOLD) signal intensity increases when humans were chased through a virtual maze (i.e., approached by a simulated predator), and these signal increases correlated with self-reported feelings of dread (Mobbs et al., 2007). The interpretation of the PAG as a center for coordinating survival-based responses has been used to unify these many observations under a single coherent function (Fanselow, 1991), in which the PAG is thought to play a central role in an evolutionarily ancient "fear circuit" (Panksepp, 2011).

A great deal of empirical evidence testing PAG function does not fall neatly under this survival-based interpretation, however. Most importantly, the PAG has been observed to play a functional role in regulating bodily processes at moments when threat is absent (for review, see Carrive, 1993), including control of the heart (e.g., interbeat interval, Gray et al., 2009; Hermans et al., 2013; Hohenschurz-Schmidt et al., 2020; Wager et al., 2009), blood pressure control (Green et al., 2005), bladder control (B. F. Blok et al., 1997; B. F. M. Blok & Holstege, 1998), rapid-eye-movement (REM) sleep (Lu et al., 2006), body temperature (Chen et al., 2002; Y. H. Zhang et al., 1997) and trigeminovascular contributions to migraine headache (Knight & Goadsby, 2001). Furthermore, PAG anatomical connectivity places it at a critical integration point in brain–body communication (Table S1; Carrive & Morgan, 2012). Evidence of PAG involvement in responses to predatory threat is consistent with the more basic role of the PAG in coordinating and regulating internal bodily systems because both fight and flight responses involve coordinating the autonomic nervous system, the endocrine system, and other systems in the body with skeletomotor movements that promote survival in critical moments. Thus, the PAG plays a more general regulatory role outside of such exceptional survival-related

circumstances (Pereira et al., 2010; Tryon & Mizumori, 2018; for review, see Benarroch, 2012; Motta et al., 2017). To estimate PAG activity under more everyday non-life-threatening circumstances, the present work used ultra-high resolution (7 Tesla; 7T) fMRI in humans to examine BOLD signal intensity in subregions of the PAG as human participants completed a simple *N*-back working memory task. In this task, participants monitored a sequence of letters presented one at a time and responded with a key press when a letter was repeated from the immediately prior trial (1-back) or three trials prior (3-back; Figure 1).

A key component of survival-based interpretations of the PAG is the attribution of specific functions to columnar subregions within the PAG (Figure 2). Functional and anatomical research in humans and non-human animals has identified dorsomedial (dmPAG), dorsolateral (dlPAG), lateral (lPAG), and ventrolateral (vlPAG) columns (Bandler, Carrive, & Depaulis, 1991; for review, see Carrive, 1993). An influential theoretical model of PAG function attributed particular survival-based functions to these columns, with dl/lPAG organizing a "circa-strike" response (i.e., a response just before/after attack), and vlPAG organizing "post-encounter" defensive responses—i.e., where a predator is detected but attack is not yet imminent (Fanselow, 1991). This work was inspired by observed differences in the behavioral and physiological consequences of dl/lPAG and vlPAG stimulation in a variety of mammalian species. For example, stimulation of dl/lPAG, in rodents and cats, increases cardiac and respiratory rates (Bandler, Carrive, & Zhang, 1991; Carrive & Bandler, 1991; Depaulis et al., 1992; Subramanian et al., 2008; W. Zhang et al., 2005), and elicits explosive running and jumping (Bandler, Carrive, & Zhang, 1991; Fardin et al., 1984; Morgan et al., 1998; S. P. Zhang et al., 1990). In contrast, stimulation of vlPAG, in rodents and cats, decreases cardiac and respiratory rates (Bandler, Carrive, & Zhang, 1991; Carrive & Bandler, 1991; Depaulis et al., 1992; Lovick, 1992; Subramanian et al., 2008), and induces an absence of movement in cats (S. P. Zhang et al., 1990) and "freezing" behavior in rats (Carrive et al., 1997; Morgan et al., 1998), where "freezing" is interpreted as a species-typical response to an anticipated or observed threat (Bolles & Fanselow, 1980). Similarly, in humans, column-level specificity could not be achieved when electrically stimulating the PAG, but blood pressure was increased by stimulating near dorsal PAG and decreased by stimulating near ventral PAG (Green et al., 2005). In both decerebrate and freely moving cats, some columnar differences are further qualified by interactions along the rostral–caudal axis of the PAG—e.g., within the rostral lPAG stimulation elicits defensive positions and

vocalization (interpreted as “flight”), while caudal lPAG stimulation elicits rapid running and jumping (interpreted as a “threat display”; Carrive, 1991; S. P. Zhang et al., 1990; for review, see Carrive, 1993).

Given these functional distinctions in subsections of the PAG, it is important for in-vivo human imaging to spatially resolve the PAG at a level of detail where columns can be distinguished. 7T brain imaging has previously distinguished the PAG from the cerebral aqueduct that it surrounds (Kragel et al., 2019; Satpute et al., 2013), but did not precisely resolve distinctions at the columnar level; for example, Kragel et al. was an early publication of initial data from this study (involving the first 24 participants who completed the study). Thus, in the present work, the larger number of participants in the total sample (N = 87) now affords us the opportunity to clearly resolve group-level distinctions at the columnar level. This allows us to test whether functional distinctions among PAG columns could be detected in non-survival-based circumstances.

In the present work, we computed and aligned subject-specific PAG masks to plot a group-level mask of PAG BOLD signal intensity during 1-back and 3-back conditions of the *N*-back working memory task. Consistent with much prior research, we expected the 3-back condition to be more difficult than the 1-back condition, as evidenced by differing hit rates (Carter et al., 1998; Jaeggi et al., 2010; Jonides et al., 1997). Consistent with Kragel et al. (2019), we expected greater PAG BOLD signal increases in the 3-back relative to the 1-back condition. However, we also expected to observe bilateral symmetry in PAG BOLD signal, as would be predicted from prior non-human animal research, which shows bilateral spatial organization within the PAG (Carrive et al., 1987; Carrive & Bandler, 1991; S. P. Zhang et al., 1990). Columnar differences in BOLD signal would suggest that functional distinctions among PAG columns are relevant outside of the threat-related scenarios that intensely activate PAG neurons. Peripheral physiology was also recorded throughout the task to validate that the 1-back and 3-back conditions elicited the expected changes in autonomic nervous system (ANS) response. Specifically, we measured phasic skin conductance response (SCR) amplitudes, cardiac interbeat interval (IBI; the time interval between successive heart beats; the inverse of heart rate (HR)), and respiration rate (RR). We expected similar signal patterns to those observed for the PAG (i.e., significant increase from baseline in both 1-back and 3-back for phasic skin conductance, HR (i.e., a decrease in IBI), and RR, and greater increases during 3 than 1-back). We also

explored the relationship between changes in BOLD signal intensities and the magnitude of ANS change (relative to baseline) rather than making specific predictions. Previous studies that have correlated ANS measures with BOLD activity in a single brain area have routinely failed to find simple correlations between the two types of signals (e.g., Beissner et al., 2013).This is likely in part because both sympathetic and parasympathetic innervation impact many peripheral physiological measures, notably HR, with multiple possible patterns of sympathetic and parasympathetic nervous system change that can lead to the same heart rate change (Berntson et al., 1993). This makes HR a complexly determined outcome, and makes mapping brain areas to HR changes difficult, if not impossible. Further, the generation and regulation of autonomic and end-organ measures (e.g., such as HR) are subserved by a larger network of regions that coordinate and regulate these ANS outputs (Bär et al., 2016; Gianaros et al., 2004; Kleckner et al., 2017; Saper, 2002); these regions include but are not limited to the PAG.

Results

Behavior significantly differed between 1-back and 3-back conditions. Behavioral results, as expected, differed between 1-back and 3-back conditions. Participants gave more correct answers (i.e., showed higher hit rates) during 1-back trials ($M = 0.992$, $SD = 0.022$), than 3-back trials ($M = 0.892$, $SD = 0.080$), $t_{(85)} = 12.18$, $p < 1e^{-15}$, $d = 1.31$. Participants also responded more quickly on 1-back trials ($M = 0.762$, $SD = 0.156$) than on 3-back trials ($M = 0.993$, $SD = 0.215$), $t_{(85)} = 13.75$, $p < 1e^{-15}$, $d = 1.48$. Response time for incorrect answers did not significantly differ between 1-back and 3-back trials.

Autonomic measures during the 1-back and 3-back conditions. Preprocessed ANS measures (see Methods) were compared to baseline (i.e., 25-second fixation period prior to each block) and participant averages were computed for the 1-back and 3-back task periods. All physiological signals differed from baseline in both 1-back and 3-back conditions, as expected, with the exception of one: IBI significantly increased from baseline during the 1-back condition, indicating that HR slowed (Table S2). However, as expected, the 3-back condition (compared to the 1-back condition) produced increased phasic electrodermal activity, $t_{(67)} = 5.69$, $p < 1e^{-6}$, $d = 0.69$, shorter cardiac interbeat intervals (IBI), $t_{(58)} = 5.21$, $p < 1e^{-5}$, $d = 0.68$, indicating a faster heart rate, and faster respiration rates, $t_{(46)} = 6.07$, $p < 1e^{-7}$, $d = 0.89$ (Figure 3).

BOLD signal intensity in the periaqueductal grey during the 1-back and 3-back conditions. PAG BOLD signal intensity, averaged across all PAG voxels, was increased during the 3-back condition relative to baseline fixation, $t_{(86)} = 2.41$, $p < 0.01$, $d = 0.26$, as expected. PAG BOLD signal intensity also increased from baseline fixation in the 1-back condition, $t_{(86)} = 1.79$, $p < 0.039$, $d = 0.19$. There was no significant difference in overall PAG BOLD signal intensity between 1-back and 3-back conditions, $t_{(86)} = 1.34$, $p < 0.091$, $d = 0.14$.

PAG BOLD signal intensity demonstrated columnar specificity. Visual inspection of BOLD signal intensity (vs. baseline fixation) in 1-back and 3-back task periods revealed what appeared to be columnar stripes that were strongest in bilateral vlPAG, and extended along the entire rostral–caudal axis (Figure 4a). To quantify this observation (see Methods), we subdivided the PAG along its radial degrees (*degree rank;* comprised of 10 ordinal ranks) and along its rostral–caudal axis (*rostral–caudal rank;* comprised of 4 ordinal ranks; Figure 4b). PAG BOLD signal intensity was averaged within subregions (combining left/right sides for this analysis) and submitted to a linear mixed-effect model including all main effects and interactions [*N*-back condition (3-back vs. 1-back) x degree rank (1-10) x rostral–caudal rank (1-4)]. We observed a significant three-way interaction [$F_{(86.00} = 5.43$ $p < 0.023$]. Within the 3-back condition, we observed significant main effects of degree rank [$F_{(86.00)} = 17.09$, $p < 1^{-4}$] and of rostral–caudal rank [$F_{(86.00)} = 24.03$, $p < 1e^{-5}$], qualified by an interaction [$F_{(86.00)} = 14.99$, $p < 0.001$], such that BOLD signal intensity increased in more lateral PAG regions (higher degree rank) [$B = 0.64$, $SE = 0.16$, $t_{(86.00)} = 4.13$, $p < 1e^{-4}$], and this positive relationship was stronger at the caudal end of the PAG. BOLD signal intensity also increased toward the rostral end of the PAG [$B = 3.86$, $SE = 0.79$, $t_{(86.00)} = 4.90$, $p < 1e^{-5}$]. Within the 1-back condition, we also observed significant main effects of degree rank [$F_{(86.00)} = 9.27$, $p < 0.01$] and rostral–caudal rank [$F_{(86.00)} = 12.14$, $p < 0.001$]. The interaction within the 1-back condition was marginally significant [$F_{(86.00)} = 3.60$, $p < 0.061$]. As in the 3-back task, BOLD signal intensity increased in more lateral PAG regions (i.e., higher degree rank) [$B = 0.34$, $SE = 0.11$, $t_{(86.00)} = 3.04$, $p < 0.01$], and this positive relationship was stronger at the caudal end of the PAG; BOLD signal intensity increased toward the rostral end of the PAG in the 1-back condition [$B = 1.81$, $SE = 0.52$, $t_{(86.00)} = 3.485$, $p < 0.001$].

Peripheral physiology reactivity correlates to novel patterns of PAG BOLD signal intensity in a working memory *N*-back task. We examined the spatial organization of PAG BOLD

signal intensity in relation to peripheral physiological changes in phasic electrodermal activity (specifically, the amplitude of skin conductance responses or SCR amplitude), cardiac interbeat interval (IBI), and respiratory rate (RR) during both task periods. Correlations were thresholded using a bootstrapped confidence interval, resampling across participants [1000 resamples], and excluding any voxel where the 95% confidence interval included zero. We observed some evidence for spatially-organized correlations across the rostral–caudal axis of the PAG (Figure 5), with IBI showing stronger correlations in medial and caudal PAG regions during the 3-back task period. Respiration showed some evidence of organization, with scattered positive correlations in medial and caudal areas. By contrast, phasic electrodermal activity showed no clear spatial pattern of correlation.

Discussion

This study shows that the human PAG is involved in regulating brain-body interactions even in the absence of painful or threatening stimuli. We observed a columnar organization of BOLD signal changes within the PAG in both a relatively cognitively demanding 3-back condition of an *N*-back memory task and a less demanding 1-back condition of the same task. These findings, particularly the changes in PAG BOLD signal during the 1-back condition, are consistent with the hypothesis that PAG neurons are continually involved in coordinating and regulating the inner systems of the body, including the autonomic nervous system. PAG circuitry may be intensely engaged during episodes involving fight-or-flight, but the circuits are not dedicated to those behaviors.

The specific pattern of findings indicated increases in BOLD signal intensity bilaterally in the ventrolateral periaqueductal gray (vlPAG) during both *N*-back conditions, (Figure 4a), with the greatest increases at the caudal pole (Figure 4b). This pattern of findings replicated an earlier 7T scanning study from our group showing an increase in ventrolateral (vlPAG) PAG BOLD signal at the caudal pole while participants viewed affectively evocative images (Satpute et al., 2013). Future research on PAG neuron activity, particularly in non-human animals during everyday circumstances with greater ecological realism, will be required to better understand the vlPAG function beyond its role in threat-related defensive behaviors.

Both *N*-back conditions elicited changes in skin conductance, IBI, and RR as predicted, with the exception of the statistically significant increase in IBI (decrease in heart rate relative to

baseline) during the 1-back condition. Skin conductance provides end-organ measures that reflect the impact of only sympathetic nervous system activity (Boucsein, 2012). Phasic skin conductance changes were somewhat correlated with PAG activity during both conditions (Figure 5), consistent with both anatomical and functional evidence that the PAG regulates sympathetic nervous system function (Bandler, Carrive, & Depaulis, 1991; Dampney et al., 2013; Keay & Bandler, 2001); in this study, the phasic skin conductance changes showed no clear spatial pattern of organization, however. IBI changes showed the strongest correlation with medial and caudal PAG activity during the 3-back condition, and respiration rate changes were similarly correlated but less so. IBI and respiratory rate changes are implemented by both the sympathetic and parasympathetic branches of the autonomic nervous system, and changes can occur due to multiple patterns of activity (e.g., decreases in IBI associated with heart rate increases can be achieved by increases in sympathetic activity plus parasympathetic withdrawal, but also via other combinations of sympathetic and parasympathetic activity as well; Berntson et al., 1994). The failure to observe strong patterns between measurements of ANS function and PAG BOLD signal was not particularly surprising to us, given that a change in any specific ANS-related signal is subserved by a larger network of regions including but not limited to the PAG, and that end-organ measurements of autonomic nervous system function (SCR amplitude, IBI, RR) may not be sensitive enough to capture what the PAG's modulation of the autonomic nervous system in non-threat conditions. Further mechanistic research on the role of the PAG in regulating specific branches of the autonomic nervous system, beyond the PAG’s relation to end-organ changes, will be required to improve our understanding of the PAG’s role in bodily regulation.

Methods

Participants. One hundred forty participants were recruited from the Greater Boston area, of which 18 withdrew participation or ended the MRI scan session before starting the working memory task. Nineteen participants were excluded due to poor signal quality (e.g., fMRI registration-failures). Sixteen participants were excluded for excessive head motion (> 0.5 mm framewise displacement in > 20% of TRs in the run; see *MRI preprocessing*). Our final sample consisted of 87 participants (M_{age} = 26.99 years, *SD* = 6.12 years; 39 female, 47 male, 1 non-response). The participant sample was 86.2% non-Hispanic, 62.1% White/Caucasian, 25.3% Asian, and 9.2% Black/African American, and generally well-educated (24.1% had some graduate education, 25.3% had completed college/university, 36.8% had some college/university, 10.3% had completed high school, and 2.3% had not completed high school). Peripheral physiological recordings were inspected for noise (see *Peripheral Physiological Recording and Quality Assessment*) and only clean recordings were included in analyses. Of the 87 participants with usable fMRI data, 68 had high-quality skin conductance data, 59 had high-quality cardiac data, and 47 had high-quality respiratory data.

All participants were between 18 and 40 years old, were right-handed, had normal or corrected to normal vision, were not pregnant, were fluent English speakers, and had no known neurological or psychiatric illnesses. Participants were excluded from participating in the study if they were claustrophobic or had any metal implants that could cause harm during scanning. All participants provided written informed consent and study procedures were completed as approved by the Partners' Healthcare Institutional Review Board.

Experimental Paradigm. Participants completed a visual *N*-back working memory task during fMRI scanning, based on the experimental design of prior studies (J. R. Gray et al., 2003; van Ast et al., 2016; Figure 1). The task was administered during a single scanning session and pseudorandomly alternated between blocks of either 1-back or 3-back conditions with 10 trials in each block. The session included a total of 12 blocks that were presented in ABBA or BAAB order (counterbalanced across participants) and were each followed by a 25-s rest period. Each block began with a cue indicating the current task (1-back or 3-back). The task was designed with fixed proportions of 20% targets and 80% nontargets (12.5% of which were lures) in each block. Lure trials were defined as 2-back matches in the 1-back blocks and lures in 3-back blocks

were either 2 or 4-back matches. The proportion of lure trials was the same for both 1-back and 3-back blocks.

On every trial, a letter (Q, W, R, S, or T) was presented at the center of the visual field for 2 s followed by a fixation cross for 2 s. Participants were instructed to respond with a button press when the letter on the screen matched the one presented *n* trials ago where *n* was either 1 or 3. The task was administered in MATLAB (RRID:SCR_001622, The MathWorks), using the Psychophysics Toolbox extensions (RRID:SCR_002881; Kleiner, 2007). Stimuli were projected so participants could view them on a mirror fixed to the head coil used for data acquisition. Responses were recorded using an MR-compatible button box. Response times and hit rates for target trials were computed using this signal and served as the primary behavioral outcomes.

Before scanning, participants completed a practice session on a laptop. These practice sessions mirrored the task used during scanning, including alternating blocks of 1-back and 3-back trials, for a total of 48 trials. The goal of the practice session was to ensure that participants were adequately familiar with the *N*-back task.

MRI Data Acquisition. Gradient-echo echo-planar imaging BOLD-fMRI was performed on a 7-Tesla (7T) Siemens MRI scanner at the Athinoula A. Martinos Center for Biomedical Imaging at Massachusetts General Hospital (MGH), Boston, MA. Functional images were acquired using GRAPPA-EPI sequence: echo time = 28 ms, repetition time = 2.34 s, flip angle = 75°, slice orientation = transversal (axial), anterior to posterior phase encoding, voxel size = 1.1 mm isotropic, gap between slices = 0 mm, number of slices = 123, field of view = 205 × 205 mm^2, GRAPPA acceleration factor = 3; echo spacing = 0.82 ms, bandwidth = 1414 Hz per pixel, partial Fourier in the phase encode direction = 7/8. A custom-built 32-channel radiofrequency coil head array was used for reception. Radiofrequency transmission was provided by a detunable band-pass birdcage coil.

Structural images were acquired using a T1-weighted EPI sequence, selected so that functional and structural images had similar spatial distortions, which facilitated co-registration and subsequent normalization of data to MNI space. Structural scan parameters were echo time = 22 ms, repetition time = 8.52 s, flip angle = 90°, number of slices = 126, slice orientation = transversal (axial), voxel size = 1.1 mm isotropic, gap between slices = 0 mm, field of view = 205 × 205 mm^2, GRAPPA acceleration factor = 3; echo spacing = 0.82 ms, bandwidth =1414 Hz per pixel, partial Fourier in the phase encode direction = 6/8.

MRI Preprocessing. MRI data were preprocessed using FMRIPREP (Esteban et al., 2019), a Nipype (Gorgolewski et al., 2011) based tool. Spatial normalization of anatomical data to the ICBM 152 Nonlinear Asymmetrical template version 2009c was performed through nonlinear registration with the antsRegistration tool of ANTs v2.1.0 (Avants et al., 2008; Gorgolewski et al., 2011), using brain-extracted versions of both T1w volume and template. Brain tissue segmentation of cerebrospinal fluid (CSF), white-matter (WM) and gray-matter (GM) was performed on the brain-extracted T1w using FAST (FMRIB's Automated Segmentation Tool; FSL v5.0.9) (Zhang et al., 2001). Functional data were slice time corrected using 3dTshift from AFNI v16.2.07 (Cox, 1996) and motion corrected using MCFLIRT (FSL v5.0.9) (Jenkinson et al., 2002). This was followed by co-registration to the corresponding T1w using boundary-based registration (Greve & Fischl, 2009) with six degrees of freedom, using FLIRT (FMRIB's Linear Image Registration Tool; FSL v5.0.9) (Jenkinson et al., 2002; Jenkinson & Smith, 2001). Motion correcting transformations, BOLD-to-T1w transformation, and T1w-to-template (MNI) warp were concatenated and applied in a single step using ants ApplyTransforms (ANTs v2.1.0) using Lanczos interpolation. Physiological noise regressors were extracted using the aCompCor method (Muschelli et al., 2014), taking the top five principle components from subject-specific CSF and WM masks, where the masks were generated by thresholding the WM/CSF masks derived from fast at 99% probability, constraining the CSF mask to the ventricles (using the ALVIN mask; Kempton et al., 2011), and eroding the WM mask using the binary_erosion function in SciPy v.1.6.1 (Virtanen et al., 2020). Frame-wise displacement (Power et al., 2014) was calculated for each functional run using the implementation of Nipype. Many internal operations of fmriprep use Nilearn (Abraham et al., 2014; RRID: SCR_001362), principally within the BOLD-processing workflow. For all participants, the quality of brain masks, tissue segmentation, and MNI registration was visually inspected for errors using the html figures provided by the fmriprep pipeline.

PAG Identification and Alignment. An additional alignment step was taken to ensure that BOLD signal estimates in the PAG were aligned across subjects using a technique developed in prior work (Kragel et al., 2019). For each subject, a semi-automated iterative procedure (described in Kragel et al., 2019) created subject-specific masks of the cerebral aqueduct by identifying high-variance voxels in the region. Following this, subject-specific PAG

masks were created by dilating the aqueduct mask (2 voxels, i.e., 2.2mm) and masking voxels in the original subject-specific aqueduct mask, voxels not in a subject-specific gray-matter segmentation (> 50% probability), and any voxels outside the target range [MNI: -22 > y > -42; z > -14]. A custom group PAG-aligned template was created using DARTEL (Ashburner, 2007), which first aligned subject-specific PAG masks in approximate MNI space, then warped whole-brain contrast images using the subject-specific transformation to the common PAG-aligned space.

The group-aligned PAG template was subdivided into columnar ROIs (Figure 2). Voxel x/y/z coordinates were submitted to PCA to identify the PAG longitudinal axis, and a geometric transformation on the remaining PCA components gave the radius and degree of each PAG voxel (relative to the y axis, at 0°). PAG columns were defined by their degree range: dorsomedial (+/- 22.5°), left/right dorsal (22.5° - 60°), left/right lateral (60° - 97.5°), and left/right ventral (97.5° - 135°), with the ventromedial quarter of the mask excluded from analysis. The ventral 90° of the PAG was excluded from analysis, given that it contains other subcortical structures (e.g., dorsal raphe). Columnar ROIs were only used for display purposes, and subdivisions of the PAG for modeling analyses (Figure 4b) are described in *Linear Mixed-Effect Model***.**

Peripheral Physiological Recording and Quality Assessment. All peripheral physiological measures were collected at 1kHz using an AD Instruments PowerLab data acquisition system with MR-compatible sensors and LabChart software. Data were continuously acquired throughout the entire scan session and partitioned for alignment with fMRI data using experimenter annotations in LabChart and scanner TR events. A piezo-electric pulse transducer (PowerLab, AD Instruments) measured heart rate from the left-hand index fingertip. A respiratory belt with a piezo-electric transducer (UFI) measured respiratory rate and was placed around the lower sternum. Non-ferrous wired Ag/AgCl electrodes containing isotonic paste on the left middle and ring fingertips measured electrodermal activity via an FE116 GSR amplifier.

Physiological time-series data were visually inspected for quality in Biopac Student Lab (Biopac Systems Inc, California, USA) and in custom visualizations using R (v.3.6.2; R Core Team, 2016) and ggplot2 (v.3.2.1; Wickham, 2009). Time-series were classified as high-quality (i.e., clean of artifacts), noisy (i.e., containing a few artifacts among periods of otherwise usable data), and unusable (i.e., containing artifacts and little to no usable data). Contamination of electrodermal signals by respiration was also noted when present, and we quantified the

percentage of the time-course that was contaminated for each participant and run. Among the 87 participants with usable fMRI data, skin conductance data was high-quality (i.e., respiratory noise was absent, and skin conductance responses or SCRs could be easily identified) for 34 participants, high-quality but with respiratory contamination (i.e., presence of any confounding respiratory noise) for 34, noisy (i.e., presence of high-frequency noise) for 8, unusable (i.e., no detectable skin conductance changes) for 8, and missing for 3. Cardiac data was high-quality (i.e., all 1-minute segments were sufficiently clear of motion to allow cardio peaks to be easily identified) for 59 participants, noisy (i.e., motion was present in < 50% of the 1-minute segments that made it difficult to identify cardio peaks) for 12, unusable (i.e., motion was present in most segments, and peaks could not easily be identified) for 14, and missing for 2. Respiratory data was high-quality (i.e., visible periodic oscillations, including asymmetric oscillations (participants breathe in, hold breath, and quickly exhale)) for 50 participants, noisy (i.e., large and frequent motion artifacts causing high-frequency noise, belt detachment, or oscillatory rates outside the range of 7-20 breaths per minute) for 20, unusable (i.e., no regular oscillatory motion could be detected, or the amplitude was so low that it could not be distinguished from noise) for 14, and missing for 3. Only high-quality time-series were used for cardiac and respiratory analyses, whereas for electrodermal activity, time-series contaminated by respiratory noise, but otherwise clean, were included on the basis that all physiological analyses involved relative comparisons against a baseline period that should be equally contaminated by the respiratory signal.

Peripheral Physiological Analysis. Physiological time-series data were analyzed using MATLAB toolboxes and custom R scripts. Heart rate was calculated using the PhysIO MATLAB toolbox (Kasper et al., 2017), which used a 0.3 to 9 Hz band-pass filter, and identified peaks using a two-pass process. The first-pass estimated run average heart rate (inverse of IBI), detecting peaks exceeding 40% of normalized amplitude, assuming a minimum peak spacing consistent with < 90 beats per minute. First-pass peaks are used to create an averaged template, and the first-pass estimated average heart rate is used as a prior to detect peaks on the second-pass (for more details, see Kasper et al., 2017). PhysIO pipeline peaks were compared with peaks identified in Biopac by trained coders. Discrepancies between the two methods were rare (0.5% of peaks across all runs and participants), and occurred more rarely in the dataset scored by a more experienced coder (0.323% of peaks), compared to the dataset scored by a less experienced

coder (0.878% of peaks). Heart rates were smoothed with a 6-second rolling average, downsampled into scan slices, and converted to IBIs. Respiratory rates were calculated using custom R scripts. A 1Hz low-pass filter was applied to the respiratory time-series, and local peaks were identified in a sliding 500ms window. To remove pseudopeaks (i.e., where participants reversed inhalation/exhalation before drawing or expelling a full breath), local peaks were removed when respiratory belt tension at that peak was within 0.5 SD of average respiratory belt tension across the entire run. Respiratory rates were smoothed with a 6-second rolling average and downsampled into scan slices. Phasic electrodermal activity was measured by the sum of amplitude peaks within each TR. All *a priori* hypotheses were tested with one-tailed t-tests.

MRI Analysis. To estimate BOLD signal intensity during the working memory *N*-back task, a general linear model was applied to preprocessed functional time-series (GLM; FSL v5.0.9). First-level models were estimated for each participant, including separate regressors for the 1-back and 3-back conditions of each trial (1 s). All regressors were convolved with a double gamma hemodynamic function. Regressors were modeled in relation to the implicit baseline of the fixation cross. Nuisance regressors included a run intercept, motion (i.e., translation/rotation in x/y/z planes, their mean-centered squares, and their temporal derivatives), aCompCor components (5 cerebral spinal fluid, 5 white matter; Muschelli et al., 2014), a discrete cosine transformation set with a minimum period of 120 seconds, and spike regressors (> 0.5mm framewise displacement; Satterthwaite et al., 2013). Group-level whole-brain contrast results were thresholded by false discovery rate ($q_{\mathrm{FDR}} < 0.05$), with a minimum cluster extent 100 voxels.

Linear Mixed-Effect Model. The spatial distribution of PAG BOLD signal intensity increases was analyzed with a linear mixed effect model, including effects of condition (1-back/3-back), rostral–caudal position rank, PAG degree rank, all interactions, by-participant random slopes, and all by-participant random intercepts. For analysis, PAG signal intensity was averaged within PAG degree and rostral–caudal position ranks. Rostral–caudal position ranks were four ordinal ranked 3.5 mm segments of the 14mm rostral–caudal axis. PAG degree ranks were ten ordinal ranked 13.5° sections of the PAG, proceeding from dorsomedial to ventrolateral sections and averaging across bilateral sections (e.g., rank 0 includes 0-13.5° in left/right PAG, while rank 9 includes 121.5-135° in left/right PAG).

Analyses were conducted in R (R Core Team, 2016) using the *lmer4* package (Bates et al., 2015), with degrees of freedom were approximated by the Scatterhwaite method, as implemented in the *lmerTest* package (Kuznetsova et al., 2017). The code was entered as follows:

```
model <- lmer(averaged PAG BOLD ~ condition × rostral–caudal position × PAG degree +
    (condition × rostral–caudal position × PAG degree | participant), control =
    lmerControl(optimizer = "bobyqa", optCtrl = list(maxfun = 2e5)))
```

Figures

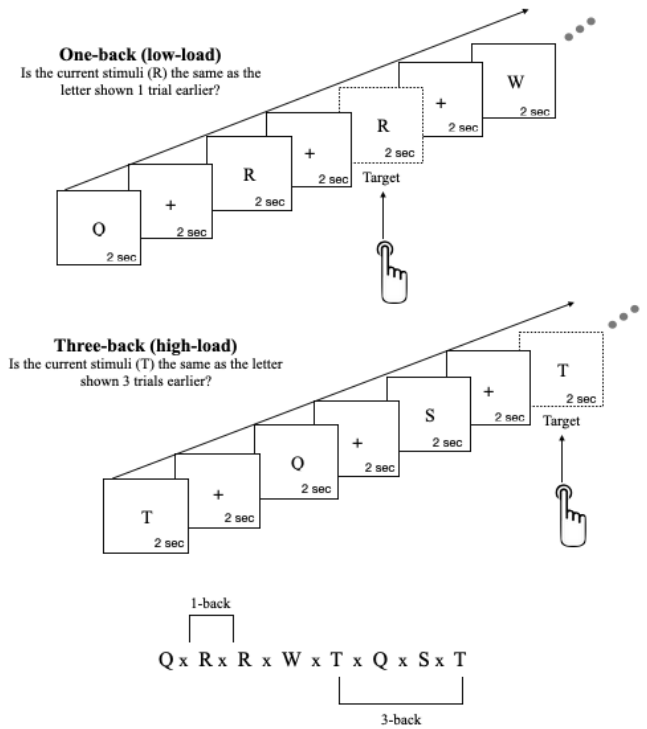

Figure 1. Schematic overview of the working memory *N*-back task.
An example of a 1-back (low-load) and 3-back (high-load) trial. For every trial, a single letter was presented at the center of the visual field for 2 seconds followed by a fixation cross for 2 seconds. Participants respond with a button press if the target stimulus matched the stimulus *n* (either 1 or 3) positions back.

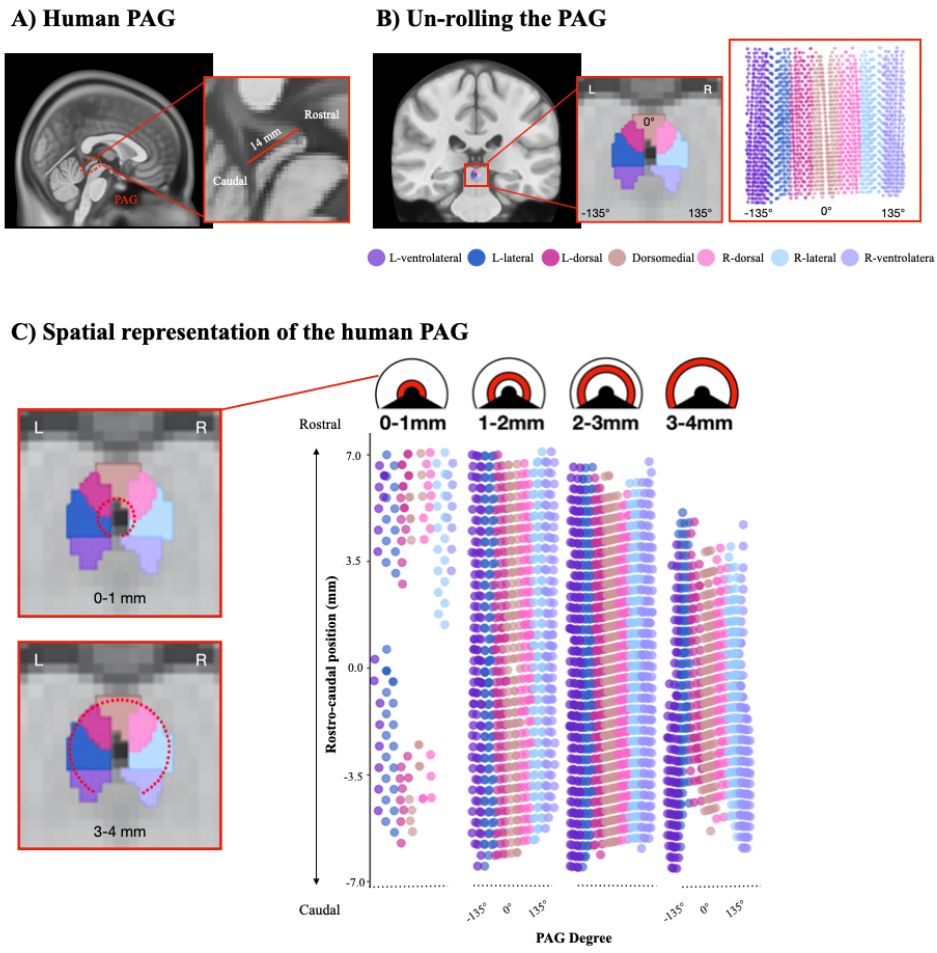

Figure 2. (A) 7-Tesla fMRI sagittal view of the human PAG. (B) Group-level template of the human PAG. The PAG template can be divided radially into 7 segments/columns (e.g., L-vlPAG, L-lPAG, L-dPAG, dmPAG, R-dPAG, R-lPAG, R-vlPG). (C) 2-D visualization of PAG voxels. Upper panels display radial cross-sections of the PAG cylinder (e.g., 0-1mm). The y-axis illustrates the longitudinal (rostral–caudal) axis of the PAG. The x-axis represents +/- 135 degrees from the brain midline (i.e., dmPAG/0°).

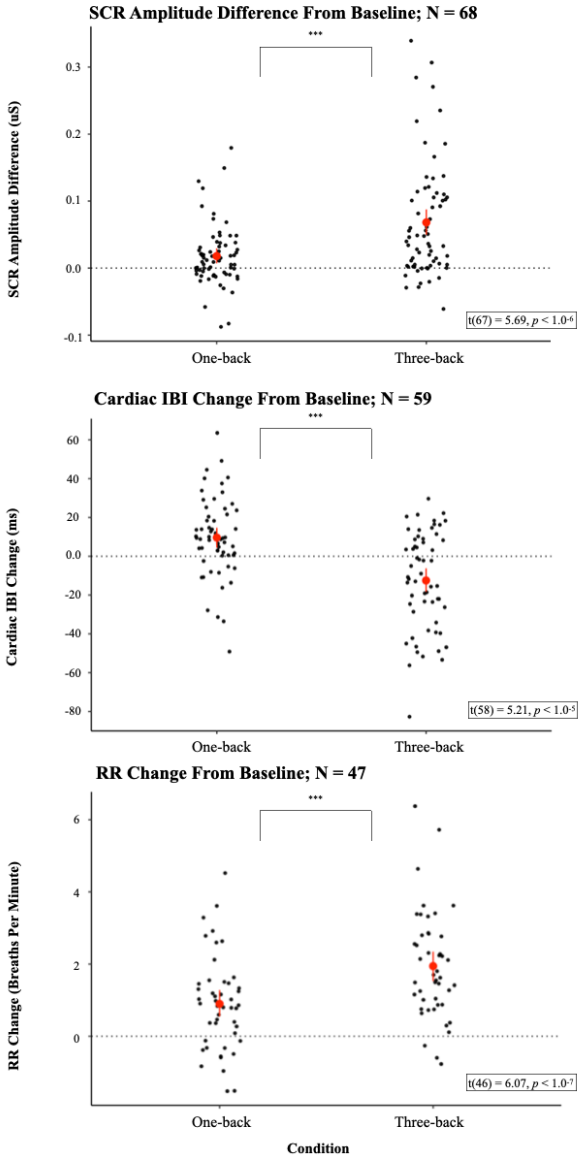

Figure 3. Mean reactivity (with a 95% confidence interval) for peripheral physiological measures during the 1-back (left) and 3-back (right) conditions of the *N*-back task. Peripheral physiological outcome measures are identified along the y-axis. Black dots illustrate skin conductance response (SCR) amplitudes (the difference between the SCR onset and SCR peak) or individual mean change scores (for IBI or RR, where each measure is a change score from baseline in measure-specific units). Red dots represent group-level means. Abbreviations: IBI: interbeat interval; RR: respiration rate; SCR: skin conductance response.

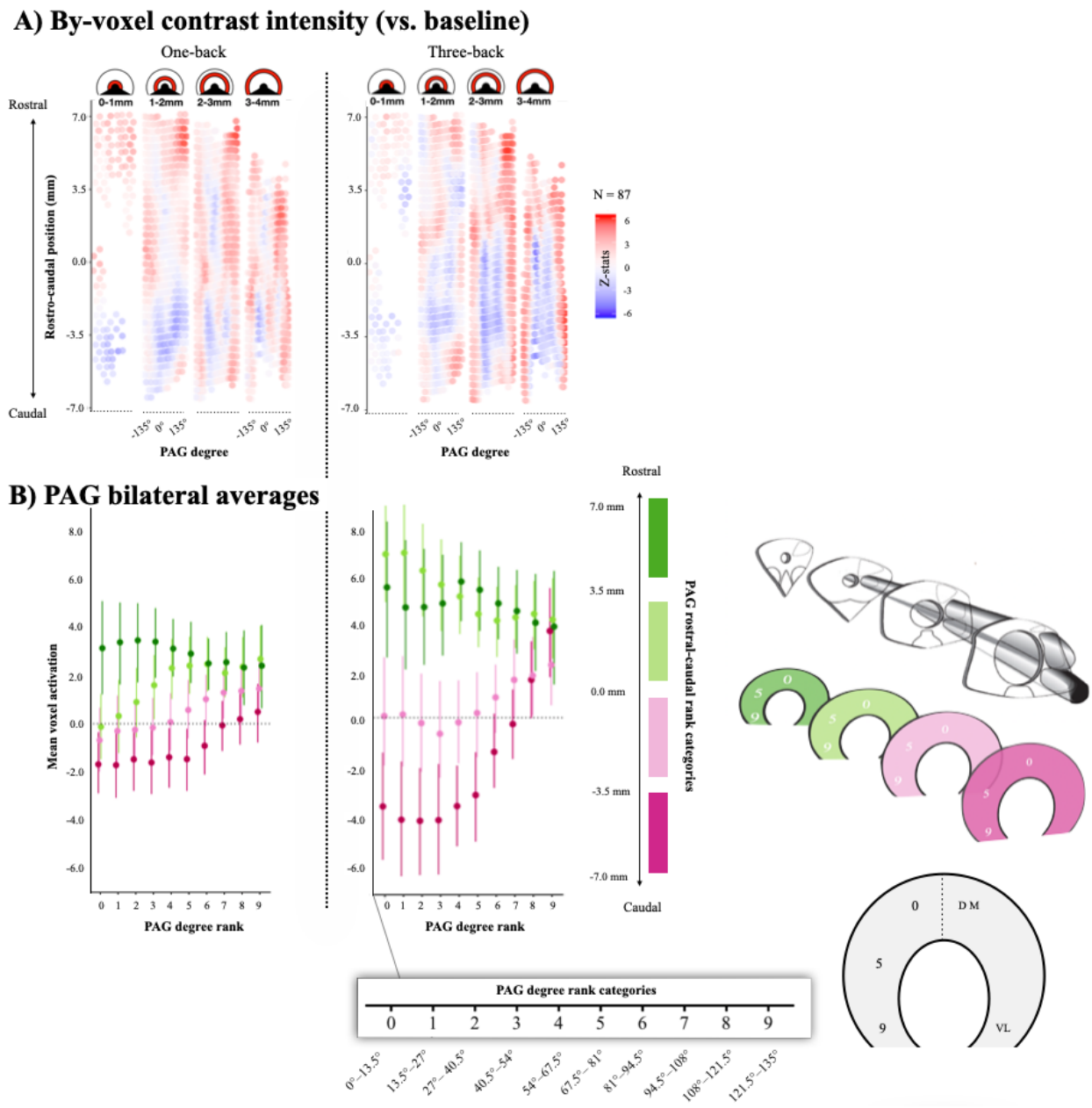

Figure 4. (A) Voxelwise PAG BOLD signal intensity during 1-back (left) and 3-back (right) conditions in the *N*-back task. Upper panels display radial cross-sections of the PAG (e.g., 0-1 mm). The y-axis illustrates voxel position along the rostral–caudal axis. The x-axis represents voxel position in degrees from the brain midline. The heat map illustrates PAG BOLD signal intensity relative to baseline fixation between task blocks. (B) Mean voxelwise activation during 1-back (left) and 3-back (right) conditions, as modeled by PAG degree and rostral–caudal position.

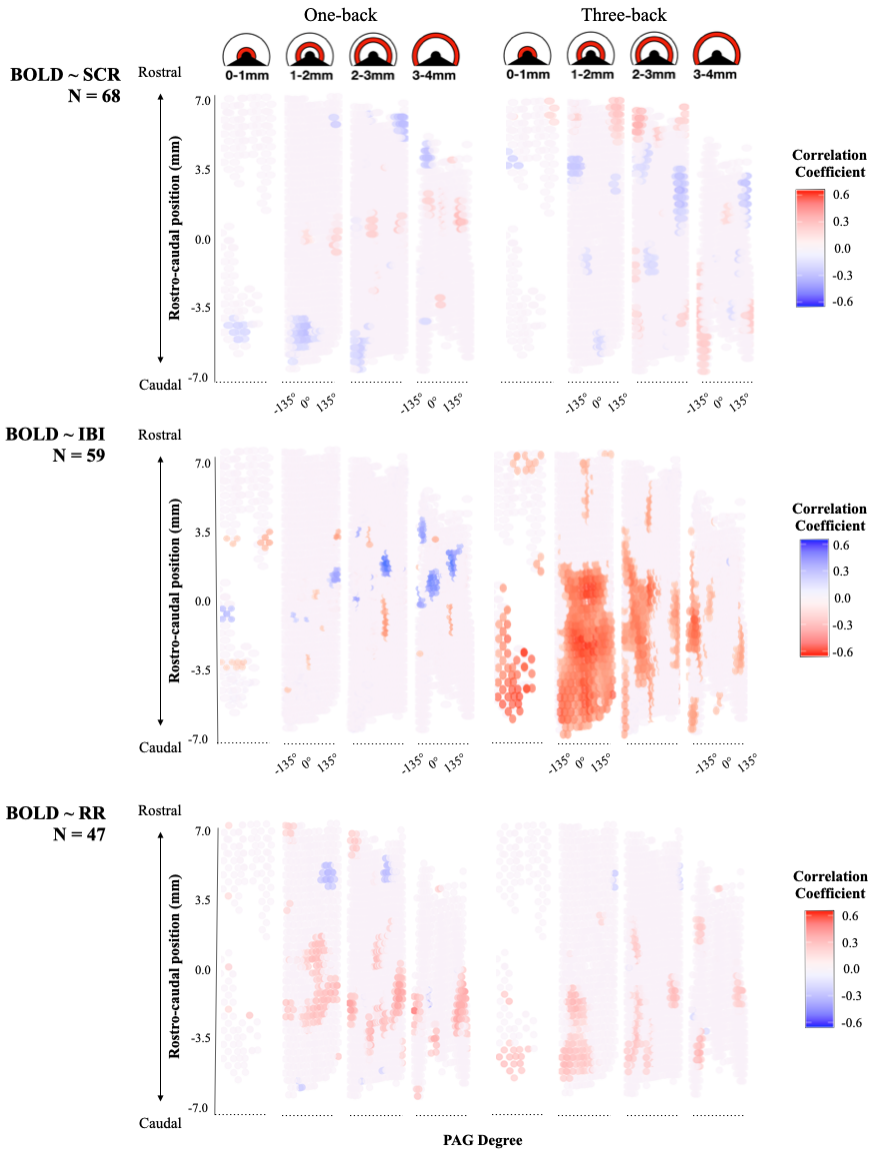

Figure 5. Cross-subject correlations between peripheral physiology voxelwise PAG BOLD signal intensity. Upper panels display radial cross-sections of the PAG cylinder (e.g., 0-1 mm). The y-axis illustrates voxel position along the rostral–caudal axis. The x-axis represents voxel position in degrees from the brain midline. The heat map illustrates magnitude (i.e., strength) of the correlation coefficients. Correlation coefficients are thresholded using bootstrap resampling across subjects within each voxel (1,000 iterations), excluding all coefficients that include 0 in a 95% confidence interval. Abbreviations: IBI: interbeat interval; RR: respiration rate; SCR: skin conductance response.

References

Abraham, A., Pedregosa, F., Eickenberg, M., Gervais, P., Mueller, A., Kossaifi, J., Gramfort, A., Thirion, B., & Varoquaux, G. (2014). Machine learning for neuroimaging with scikit-learn. *Frontiers in Neuroinformatics*, *8*. https://doi.org/10.3389/fninf.2014.00014

Abrahams, V. C., Hilton, S. M., & Zbrożyna, A. (1960). Active muscle vasodilatation produced by stimulation of the brain stem: Its significance in the defence reaction. *The Journal of Physiology*, *154*(3), 491–513.

Amano, K., Tanikawa, T., Iseki, H., Kawabatake, H., Notani, M., Kawamura, H., & Kitamura, K. (1978). Single Neuron Analysis of the Human Midbrain Tegmentum. *Stereotactic and Functional Neurosurgery*, *41*(1–4), 66–78. https://doi.org/10.1159/000102402

Ashburner, J. (2007). A fast diffeomorphic image registration algorithm. *NeuroImage*, *38*(1), 95–113. https://doi.org/10.1016/j.neuroimage.2007.07.007

Avants, B. B., Epstein, C. L., Grossman, M., & Gee, J. C. (2008). Symmetric diffeomorphic image registration with cross-correlation: Evaluating automated labeling of elderly and neurodegenerative brain. *Medical Image Analysis*, *12*(1), 26–41. https://doi.org/10.1016/j.media.2007.06.004

Bandler, R. (1988). Brain mechanisms of aggression as revealed by electrical and chemical stimulation: Suggestion of a central role for the midbrain periaqueductal grey region. In *Progress in psychobiology and physiological psychology, Vol. 13* (pp. 67–154). Academic Press.

Bandler, R., & Carrive, P. (1988). Integrated defence reaction elicited by excitatory amino acid microinjection in the midbrain periaqueductal grey region of the unrestrained cat. *Brain Research*, *439*(1–2), 95–106. https://doi.org/10.1016/0006-8993(88)91465-5

Bandler, R., Carrive, P., & Depaulis, A. (1991). Emerging Principles of Organization of the Midbrain Periaqueductal Gray Matter. In A. Depaulis & R. Bandler (Eds.), *The Midbrain Periaqueductal Gray Matter: Functional, Anatomical, and Neurochemical Organization* (pp. 1–8). Springer US. https://doi.org/10.1007/978-1-4615-3302-3_1

Bandler, R., Carrive, P., & Zhang, S. P. (1991). Integration of somatic and autonomic reactions within the midbrain periaqueductal grey: Viscerotopic, somatotopic and functional organization. *Progress in Brain Research*, *87*, 269–305. https://doi.org/10.1016/s0079-6123(08)63056-3

Bär, K.-J., De La Cruz, F., Schumann, A., Koehler, S., Sauer, H., Critchley, H., & Wagner, G. (2016). Functional connectivity and network analysis of midbrain and brainstem nuclei. *NeuroImage*, *134*. https://doi.org/10.1016/j.neuroimage.2016.03.071

Bates, D., Mächler, M., Bolker, B., & Walker, S. (2015). Fitting Linear Mixed-Effects Models Using lme4. *Journal of Statistical Software*, *67*(1), Article 1. https://doi.org/10.18637/jss.v067.i01

Beissner, F., Meissner, K., Bär, K.-J., & Napadow, V. (2013). The Autonomic Brain: An Activation Likelihood Estimation Meta-Analysis for Central Processing of Autonomic Function. *Journal of Neuroscience*, *33*(25), 10503–10511. https://doi.org/10.1523/JNEUROSCI.1103-13.2013

Benarroch, E. E. (2012). Periaqueductal gray: An interface for behavioral control. *Neurology*, *78*(3), 210–217. https://doi.org/10.1212/WNL.0b013e31823fcdee

Benedek, M., & Kaernbach, C. (2010). Decomposition of skin conductance data by means of nonnegative deconvolution. *Psychophysiology*, *47*(4), 647–658. https://doi.org/10.1111/j.1469-8986.2009.00972.x

Berntson, G., Cacioppo, J., & Quigley, K. (1993). Cardiac Psychophysiology and Autonomic Space in Humans—Empirical-Perspectives and Conceptual Implications. *Psychological Bulletin*, *114*, 296–322. https://doi.org/10.1037//0033-2909.114.2.296

Berntson, G. G., Cacioppo, J. T., Quigley, K. S., & Fabro, V. T. (1994). Autonomic space and psychophysiological response. *Psychophysiology*, *31*(1), 44–61. https://doi.org/10.1111/j.1469-8986.1994.tb01024.x

Blok, B. F. M., & Holstege, G. (1998). The central nervous system control of micturition in cats and humans. *Behavioural Brain Research*, *92*(2), 119–125. https://doi.org/10.1016/S0166-4328(97)00184-8

Blok, B. F., Willemsen, A. T., & Holstege, G. (1997). A PET study on brain control of micturition in humans. *Brain: A Journal of Neurology*, *120 (Pt 1)*, 111–121. https://doi.org/10.1093/brain/120.1.111

Bolles, R. C., & Fanselow, M. S. (1980). A perceptual-defensive-recuperative model of fear and pain. *Behavioral and Brain Sciences*, *3*(2), 291–301. https://doi.org/10.1017/S0140525X0000491X

Boucsein, W. (2012). *Electrodermal Activity*. Springer Science & Business Media.

Carrive, P. (1991). Functional Organization of PAG Neurons Controlling Regional Vascular Beds. In A. Depaulis & R. Bandler (Eds.), *The Midbrain Periaqueductal Gray Matter: Functional, Anatomical, and Neurochemical Organization* (pp. 67–100). Springer US. https://doi.org/10.1007/978-1-4615-3302-3_6

Carrive, P. (1993). The periaqueductal gray and defensive behavior: Functional representation and neuronal organization. *Behavioural Brain Research*, *58*(1–2), 27–47. https://doi.org/10.1016/0166-4328(93)90088-8

Carrive, P., & Bandler, R. (1991). Viscerotopic organization of neurons subserving hypotensive reactions within the midbrain periaqueductal grey: A correlative functional and anatomical study. *Brain Research*, *541*(2), 206–215. https://doi.org/10.1016/0006-8993(91)91020-2

Carrive, P., Dampney, R. A., & Bandler, R. (1987). Excitation of neurones in a restricted portion of the midbrain periaqueductal grey elicits both behavioural and cardiovascular components of the defence reaction in the unanaesthetised decerebrate cat. *Neuroscience Letters*, *81*(3), 273–278. https://doi.org/10.1016/0304-3940(87)90395-8

Carrive, P., Leung, P., Harris, J., & Paxinos, G. (1997). Conditioned fear to context is associated with increased Fos expression in the caudal ventrolateral region of the midbrain periaqueductal gray. *Neuroscience*, *78*(1), 165–177. https://doi.org/10.1016/S0306-4522(97)83047-3

Carrive, P., & Morgan, M. M. (2012). Periaqueductal Gray. In G. Paxinos & J. K. Mai (Eds.), *The Human Nervous System (Second Edition)* (pp. 367–400). Elsevier. https://doi.org/10.1016/B978-012547626-3/50013-2

Carter, C. S., Perlstein, W., Ganguli, R., Brar, J., Mintun, M., & Cohen, J. D. (1998). Functional Hypofrontality and Working Memory Dysfunction in Schizophrenia. *American Journal of Psychiatry*, *155*(9), 1285–1287. https://doi.org/10.1176/ajp.155.9.1285

Chen, X.-M., Nishi, M., Taniguchi, A., Nagashima, K., Shibata, M., & Kanosue, K. (2002). The caudal periaqueductal gray participates in the activation of brown adipose tissue in rats. *Neuroscience Letters*, *331*(1), 17–20. https://doi.org/10.1016/S0304-3940(02)00757-7

Cox, R. W. (1996). AFNI: Software for Analysis and Visualization of Functional Magnetic Resonance Neuroimages. *Computers and Biomedical Research*, *29*(3), 162–173. https://doi.org/10.1006/cbmr.1996.0014

Dampney, R. A. L., Furlong, T. M., Horiuchi, J., & Iigaya, K. (2013). Role of dorsolateral periaqueductal grey in the coordinated regulation of cardiovascular and respiratory function. *Autonomic Neuroscience*, *175*(1–2), 17–25. https://doi.org/10.1016/j.autneu.2012.12.008

Depaulis, A., Keay, K. A., & Bandler, R. (1992). Longitudinal neuronal organization of defensive reactions in the midbrain periaqueductal gray region of the rat. *Experimental Brain Research*, *90*(2), 307–318. https://doi.org/10.1007/BF00227243

Esteban, O., Markiewicz, C. J., Blair, R. W., Moodie, C. A., Isik, A. I., Erramuzpe, A., Kent, J. D., Goncalves, M., DuPre, E., Snyder, M., Oya, H., Ghosh, S. S., Wright, J., Durnez, J., Poldrack, R. A., & Gorgolewski, K. J. (2019). fMRIPrep: A robust preprocessing pipeline for functional MRI. *Nature Methods*, *16*(1), 111–116. https://doi.org/10.1038/s41592-018-0235-4

Fanselow, M. S. (1991). The Midbrain Periaqueductal Gray as a Coordinator of Action in Response to Fear and Anxiety. In A. Depaulis & R. Bandler (Eds.), *The Midbrain Periaqueductal Gray Matter* (pp. 151–173). Plenum Publishing Corp. https://doi.org/10.1007/978-1-4615-3302-3_10

Fardin, V., Oliveras, J.-L., & Besson, J.-M. (1984). A reinvestigation of the analgesic effects induced by stimulation of the periaqueductal gray matter in the rat. I. The production of behavioral side effects together with analgesia. *Brain Research*, *306*(1), 105–123. https://doi.org/10.1016/0006-8993(84)90360-3

Gianaros, P. J., Van Der Veen, F. M., & Jennings, J. R. (2004). Regional cerebral blood flow correlates with heart period and high-frequency heart period variability during working-memory tasks: Implications for the cortical and subcortical regulation of cardiac autonomic activity. *Psychophysiology*, *41*(4), 521–530. https://doi.org/10.1111/1469-8986.2004.00179.x

Gorgolewski, K., Burns, C. D., Madison, C., Clark, D., Halchenko, Y. O., Waskom, M. L., & Ghosh, S. S. (2011). Nipype: A Flexible, Lightweight and Extensible Neuroimaging Data Processing Framework in Python. *Frontiers in Neuroinformatics*, *0*. https://doi.org/10.3389/fninf.2011.00013

Gray, J. R., Chabris, C. F., & Braver, T. S. (2003). Neural mechanisms of general fluid intelligence. *Nature Neuroscience*, *6*(3), 316–322. https://doi.org/10.1038/nn1014

Gray, M. A., Rylander, K., Harrison, N. A., Wallin, B. G., & Critchley, H. D. (2009). Following One's Heart: Cardiac Rhythms Gate Central Initiation of Sympathetic Reflexes. *Journal of Neuroscience*, *29*(6), 1817–1825. https://doi.org/10.1523/JNEUROSCI.3363-08.2009

Green, A. L., Wang, S., Owen, S. L. F., Xie, K., Liu, X., Paterson, D. J., Stein, J. F., Bain, P. G., & Aziz, T. Z. (2005). Deep brain stimulation can regulate arterial blood pressure in awake humans. *NeuroReport*, *16*(16), 1741–1745. https://doi.org/10.1097/01.wnr.0000183904.15773.47

Greve, D. N., & Fischl, B. (2009). Accurate and robust brain image alignment using boundary-based registration. *NeuroImage*, *48*(1), 63–72. https://doi.org/10.1016/j.neuroimage.2009.06.060

Hermans, E. J., Henckens, M. J. A. G., Roelofs, K., & Fernández, G. (2013). Fear bradycardia and activation of the human periaqueductal grey. *NeuroImage*, *66*, 278–287. https://doi.org/10.1016/j.neuroimage.2012.10.063

Hohenschurz-Schmidt, D. J., Calcagnini, G., Dipasquale, O., Jackson, J. B., Medina, S., O'Daly, O., O'Muircheartaigh, J., de Lara Rubio, A., Williams, S. C. R., McMahon, S. B., Makovac, E., & Howard, M. A. (2020). Linking Pain Sensation to the Autonomic Nervous System: The Role of the Anterior Cingulate and Periaqueductal Gray Resting-State Networks. *Frontiers in Neuroscience*, *14*. https://www.frontiersin.org/articles/10.3389/fnins.2020.00147

Jaeggi, S. M., Buschkuehl, M., Perrig, W. J., & Meier, B. (2010). The concurrent validity of the N-back task as a working memory measure. *Memory (Hove, England)*, *18*(4), 394–412. https://doi.org/10.1080/09658211003702171

Jenkinson, M., Bannister, P., Brady, M., & Smith, S. (2002). Improved Optimization for the Robust and Accurate Linear Registration and Motion Correction of Brain Images. *NeuroImage*, *17*(2), 825–841. https://doi.org/10.1006/nimg.2002.1132

Jenkinson, M., & Smith, S. (2001). A global optimisation method for robust affine registration of brain images. *Medical Image Analysis*, *5*(2), 143–156. https://doi.org/10.1016/S1361-8415(01)00036-6

Jonides, J., Schumacher, E. H., Smith, E. E., Lauber, E. J., Awh, E., Minoshima, S., & Koeppe, R. A. (1997). Verbal Working Memory Load Affects Regional Brain Activation as Measured by PET. *Journal of Cognitive Neuroscience*, *9*(4), 462–475. https://doi.org/10.1162/jocn.1997.9.4.462

Kasper, L., Bollmann, S., Diaconescu, A. O., Hutton, C., Heinzle, J., Iglesias, S., Hauser, T. U., Sebold, M., Manjaly, Z.-M., Pruessmann, K. P., & Stephan, K. E. (2017). The PhysIO Toolbox for Modeling Physiological Noise in fMRI Data. *Journal of Neuroscience Methods*, *276*, 56–72. https://doi.org/10.1016/j.jneumeth.2016.10.019

Keay, K. A., & Bandler, R. (2001). Parallel circuits mediating distinct emotional coping reactions to different types of stress. *Neuroscience & Biobehavioral Reviews*, *25*(7), 669–678. https://doi.org/10.1016/S0149-7634(01)00049-5

Kempton, M. J., Underwood, T. S. A., Brunton, S., Stylios, F., Schmechtig, A., Ettinger, U., Smith, M. S., Lovestone, S., Crum, W. R., Frangou, S., Williams, S. C. R., & Simmons, A. (2011). A comprehensive testing protocol for MRI neuroanatomical segmentation techniques: Evaluation of a novel lateral ventricle segmentation method. *NeuroImage*, *58*(4), 1051–1059. https://doi.org/10.1016/j.neuroimage.2011.06.080

Kleckner, I. R., Zhang, J., Touroutoglou, A., Chanes, L., Xia, C., Simmons, W. K., Quigley, K. S., Dickerson, B. C., & Feldman Barrett, L. (2017). Evidence for a large-scale brain system supporting allostasis and interoception in humans. *Nature Human Behaviour*, *1*, 0069. https://doi.org/10.1038/s41562-017-0069

Kleiner, M. (2007). *What's new in Psychtoolbox-3?* 89.

Knight, Y. E., & Goadsby, P. J. (2001). The periaqueductal grey matter modulates trigeminovascular input: A role in migraine?11Presented in part at the Xth International Headache Congress, Barcelona, Spain, 24–26 June 1999 [Knight and Goadsby, Cephalalgia 19 (1999) 315]. *Neuroscience*, *106*(4), 793–800. https://doi.org/10.1016/S0306-4522(01)00303-7

Kragel, P. A., Bianciardi, M., Hartley, L., Matthewson, G., Choi, J.-K., Quigley, K. S., Wald, L. L., Wager, T. D., Barrett, L. F., & Satpute, A. B. (2019). Functional Involvement of Human Periaqueductal Gray and Other Midbrain Nuclei in Cognitive Control. *Journal of Neuroscience*, *39*(31), 6180–6189. https://doi.org/10.1523/JNEUROSCI.2043-18.2019

Kuznetsova, A., Brockhoff, P. B., & Christensen, R. H. B. (2017). lmerTest Package: Tests in Linear Mixed Effects Models. *Journal of Statistical Software*, *82*(1), Article 1. https://doi.org/10.18637/jss.v082.i13

Lovick, T. A. (1992). Inhibitory modulation of the cardiovascular defence response by the ventrolateral periaqueductal grey matter in rats. *Experimental Brain Research*, *89*(1), 133–139. https://doi.org/10.1007/BF00229010

Lu, J., Sherman, D., Devor, M., & Saper, C. B. (2006). A putative flip–flop switch for control of REM sleep. *Nature*, *441*(7093), Article 7093. https://doi.org/10.1038/nature04767

Mobbs, D., Petrovic, P., Marchant, J. L., Hassabis, D., Weiskopf, N., Seymour, B., Dolan, R. J., & Frith, C. D. (2007). When Fear Is Near: Threat Imminence Elicits Prefrontal-Periaqueductal Gray Shifts in Humans. *Science*, *317*(5841), 1079–1083. https://doi.org/10.1126/science.1144298

Morgan, M. M., Whitney, P. K., & Gold, M. S. (1998). Immobility and flight associated with antinociception produced by activation of the ventral and lateral/dorsal regions of the rat periaqueductal gray. *Brain Research*, *804*(1), 159–166. https://doi.org/10.1016/S0006-8993(98)00669-6

Motta, S. C., Carobrez, A. P., & Canteras, N. S. (2017). The periaqueductal gray and primal emotional processing critical to influence complex defensive responses, fear learning and

reward seeking. *Neuroscience & Biobehavioral Reviews*, *76*, 39–47. https://doi.org/10.1016/j.neubiorev.2016.10.012

Muschelli, J., Nebel, M. B., Caffo, B. S., Barber, A. D., Pekar, J. J., & Mostofsky, S. H. (2014). Reduction of motion-related artifacts in resting state fMRI using aCompCor. *NeuroImage*, *96*, 22–35. https://doi.org/10.1016/j.neuroimage.2014.03.028

Nashold, B. S., Wilson, W. P., & Slaughter, D. G. (1969). Sensations evoked by stimulation in the midbrain of man. *Journal of Neurosurgery*, *30*(1), 14–24. https://doi.org/10.3171/jns.1969.30.1.0014

Panksepp, J. (2011). The basic emotional circuits of mammalian brains: Do animals have affective lives? *Neuroscience & Biobehavioral Reviews*, *35*(9), 1791–1804. https://doi.org/10.1016/j.neubiorev.2011.08.003

Pereira, E. A. C., Lu, G., Wang, S., Schweder, P. M., Hyam, J. A., Stein, J. F., Paterson, D. J., Aziz, T. Z., & Green, A. L. (2010). Ventral periaqueductal grey stimulation alters heart rate variability in humans with chronic pain. *Experimental Neurology*, *223*(2), 574–581. https://doi.org/10.1016/j.expneurol.2010.02.004

Power, J. D., Mitra, A., Laumann, T. O., Snyder, A. Z., Schlaggar, B. L., & Petersen, S. E. (2014). Methods to detect, characterize, and remove motion artifact in resting state fMRI. *NeuroImage*, *84*, 320–341. https://doi.org/10.1016/j.neuroimage.2013.08.048

R Core Team. (2016). *R: A language and environment for statistical computing*. R Foundation for Statistical Computing. https://www.R-project.org

Saper, C. B. (2002). The Central Autonomic Nervous System: Conscious Visceral Perception and Autonomic Pattern Generation. *Annual Review of Neuroscience*, *25*(1), 433–469. https://doi.org/10.1146/annurev.neuro.25.032502.111311

Satpute, A. B., Wager, T. D., Cohen-Adad, J., Bianciardi, M., Choi, J.-K., Buhle, J. T., Wald, L. L., & Barrett, L. F. (2013). Identification of discrete functional subregions of the human periaqueductal gray. *Proceedings of the National Academy of Sciences*, *110*(42), 17101–17106. https://doi.org/10.1073/pnas.1306095110

Satterthwaite, T. D., Elliott, M. A., Gerraty, R. T., Ruparel, K., Loughead, J., Calkins, M. E., Eickhoff, S. B., Hakonarson, H., Gur, R. C., Gur, R. E., & Wolf, D. H. (2013). An improved framework for confound regression and filtering for control of motion artifact in the preprocessing of resting-state functional connectivity data. *NeuroImage*, *64*, 240–256. https://doi.org/10.1016/j.neuroimage.2012.08.052

Skultety, F. M. (1963). Stimulation of Periaqueductal Gray and Hypothalamus. *Archives of Neurology*, *8*(6), 608–620. https://doi.org/10.1001/archneur.1963.00460060038004

Subramanian, H. H., Balnave, R. J., & Holstege, G. (2008). The Midbrain Periaqueductal Gray Control of Respiration. *Journal of Neuroscience*, *28*(47), 12274–12283. https://doi.org/10.1523/JNEUROSCI.4168-08.2008

Tryon, V. L., & Mizumori, S. J. Y. (2018). A Novel Role for the Periaqueductal Gray in Consummatory Behavior. *Frontiers in Behavioral Neuroscience*, *12*, 178–178. PubMed. https://doi.org/10.3389/fnbeh.2018.00178

van Ast, V. A., Spicer, J., Smith, E. E., Schmer-Galunder, S., Liberzon, I., Abelson, J. L., & Wager, T. D. (2016). Brain Mechanisms of Social Threat Effects on Working Memory. *Cerebral Cortex (New York, N.Y.: 1991)*, *26*(2), 544–556. https://doi.org/10.1093/cercor/bhu206

Virtanen, P., Gommers, R., Oliphant, T. E., Haberland, M., Reddy, T., Cournapeau, D., Burovski, E., Peterson, P., Weckesser, W., Bright, J., van der Walt, S. J., Brett, M.,

Wilson, J., Millman, K. J., Mayorov, N., Nelson, A. R. J., Jones, E., Kern, R., Larson, E., … van Mulbregt, P. (2020). SciPy 1.0: Fundamental algorithms for scientific computing in Python. *Nature Methods*, *17*(3), 261–272. https://doi.org/10.1038/s41592-019-0686-2

Wager, T. D., van Ast, V. A., Hughes, B. L., Davidson, M. L., Lindquist, M. A., & Ochsner, K. N. (2009). Brain mediators of cardiovascular responses to social threat, Part II: Prefrontal-subcortical pathways and relationship with anxiety. *NeuroImage*, *47*(3), 836–851. https://doi.org/10.1016/j.neuroimage.2009.05.044

Wickham, H. (2009). *ggplot2: Elegant Graphics for Data Analysis*. Springer-Verlag. https://doi.org/10.1007/978-0-387-98141-3

Zhang, S. P., Bandler, R., & Carrive, P. (1990). Flight and immobility evoked by excitatory amino acid microinjection within distinct parts of the subtentorial midbrain periaqueductal gray of the cat. *Brain Research*, *520*(1–2), 73–82. https://doi.org/10.1016/0006-8993(90)91692-a

Zhang, W., Hayward, L. F., & Davenport, P. W. (2005). Respiratory muscle responses elicited by dorsal periaqueductal gray stimulation in rats. *American Journal of Physiology-Regulatory, Integrative and Comparative Physiology*, *289*(5), R1338–R1347. https://doi.org/10.1152/ajpregu.00828.2004

Zhang, Y., Brady, M., & Smith, S. (2001). Segmentation of brain MR images through a hidden Markov random field model and the expectation-maximization algorithm. *IEEE Transactions on Medical Imaging*, *20*(1), 45–57. https://doi.org/10.1109/42.906424

Zhang, Y. H., Hosono, T., Yanase-Fujiwara, M., Chen, X. M., & Kanosue, K. (1997). Effect of midbrain stimulations on thermoregulatory vasomotor responses in rats. *The Journal of Physiology*, *503 (Pt 1)*, 177–186. https://doi.org/10.1111/j.1469-7793.1997.177bi.x

Supplemental Information

7-Tesla evidence for columnar and rostral–caudal organization of the human periaqueductal grey response in the absence of threat: a working memory study.

Alexandra K. Fischbach[1], Ajay B. Satpute[1, 4], Karen S. Quigley[1, 7], Philip A. Kragel[2, 3], Marta Bianciardi[4], Lawrence L. Wald[4], Tor D. Wager[6], Lisa Feldman Barrett[1, 4, 5*], Jordan E. Theriault[1,4*]

*Shared senior authorship

PAG Afferent Connections					
Region	**Sub-region**	**DM**	**DL**	**L**	**VL**
Amygdala	Anterior amygdaloid nuclei				Rabbit[3]
Amygdala	Central amygdaloid nuclei	Cat[1], Monkey[2], Rabbit[3]	Cat[1], Rabbit[3]	Monkey[2], Rabbit[3], Rat[4]	Cat[1], Monkey[2], Rabbit[3]
Amygdala	Medial amygdaloids nuclei	Rabbit[3]	Rabbit[3]	Rabbit[3]	Rabbit[3]
Amygdala	Ventrolateral basal nucleus of the amygdala		Monkey[2]	Monkey[2]	
Basal Ganglia	Globus pallidus				Rabbit[3]
Cerebellum	Dentate nucleus	Rabbit[3]	Rabbit[3]	Rabbit[3]	Rabbit[3]
Cerebellum	Fastigial nucleus				Mouse[5], Rabbit[3]
Cerebellum	Interpositus nucleus				Rabbit[3]
Cingulate	Anterior cingulate				Rat[8]
Cingulate	Anterior cingulate area 24	Monkey[2]		Monkey[2]	Monkey[2], Rat[6]
Cingulate	Dorsal anterior cingulate cortex		Rat[7]	Rat[7]	Rat[7]
Cingulate	Intermediate anterior cingulate	Rat[9]	Rat[9]		Rat[9]
Cingulate	Ventral anterior cingulate cortex		Rat[7]		Rat[7]
Frontal Lobe	Primary motor cortex				Rat[8]
Hippocampus	Hippocampus	*Not present*			
Hypothalamus	Anterior hypothalamic nuclei				Rat[8]
Hypothalamus	Anterior hypothalamus			Rat[10]	
Hypothalamus	Dorsal premammillary nucleus	Rabbit[3], Rat[11]	Rabbit[3], Rat[11,12]	Rabbit[3,12]	Rabbit[3], Rat[11,8]
Hypothalamus	Dorsomedial hypothalamus	Rabbit[3], Rat[13]	Rabbit[3], Rat[13,12]	Rabbit[3], Rat[13,12]	Rat[13]
Hypothalamus	Lateral hypothalamus			Rat[12]	Rabbit[3], Rat[8]
Hypothalamus	Medial preoptic nuclei	Rabbit[3], Rat[4]	Rabbit[3]	Rabbit[3], Rat[4]	Rat[48]
Hypothalamus	Parasubthalamic nuclei				Rat[8]
Hypothalamus	Periventricular nucleus				Rabbit[3]
Hypothalamus	Preoptic nuclei				Rabbit[3]
Hypothalamus	Retrochiasmatic area				Rat[8]
Hypothalamus	Supramammillary nucleus			Rat[12]	Rabbit[3], Rat[12]
Hypothalamus	Supraoptic nucleus			Rabbit[3]	Rabbit[3]
Hypothalamus	Ventromedial nucleus				Rat[8]
Insular Cortex	Dorsal insular cortex		Rat[7]	Rat[7]	Rat[7]
Insular Cortex	Insular cortex				Rat[6]
Insular Cortex	Posterior insular cortex				Rat[78]
Insular Cortex	Rostral insular cortex	Rabbit[3]	Rabbit[3]	Rabbit[3]	
Lateral Sulcus	Insular cortex				Rat[6]
Locus Coeruleus	Locus coeruleus				Monkey[23]
Medial Frontal Cortex	Supplementary eye field	Monkey[14]	Monkey[14]		Monkey[14]
Medial Olfactory Area	Lateral septum	Monkey[15]	Monkey[15]		
Medial Olfactory Area	Ventral septum	Monkey[15]	Monkey[15]		
Medial Prefrontal Cortex	Dorsomedial prefrontal cortex		Monkey[21]		

Medial Prefrontal Cortex	Dorsomedial prefrontal cortex area 24	Rabbit[3]	Rabbit[3]	Rabbit[3]	Rabbit[3]
Medial Prefrontal Cortex	Dorsomedial prefrontal cortex area 24b			Monkey[2]	
Medial Prefrontal Cortex	Dorsomedial prefrontal cortex area 9			Monkey[2]	
Medial Prefrontal Cortex	Medial prefrontal area 25		Monkey[2,16,17]		Monkey[2]
Medial Prefrontal Cortex	Medial prefrontal area 32	Monkey[2], Rabbit[3]	Monkey[2,16], Rabbit[3]	Rabbit[3]	Rabbit[3], Rat[6]
Medial Prefrontal Cortex	Medial prefrontal cortex	Mouse[18]	Monkey[19], Mouse[18], Rat[20]	Mouse[18]	Rat[20]
Medulla Oblongata	Lateral cervical nucleus				Rabbit[3]
Medulla Oblongata	Nucleus paragigantocellularis				Rabbit[3]
Medulla Oblongata	Raphe obscurus nucleus				Rabbit[3]
Medulla Oblongata	Solitary nucleus				Rabbit[3], Rat[22]
Medulla Oblongata	Spinal trigeminal nucleus				Rabbit[3]
Olfactory Bulb	Olfactory bulb				Rat[6]
Olfactory Cortex	Anterior olfactory cortex				Rat[6]
Orbital Cortex	Dorsolateral orbital cortex		Rat[7]	Rat[7]	Rat[7]
Orbital Cortex	Medial orbital cortex				Rat[7]
Orbital Cortex	Orbital area 12o		Monkey[2]		Monkey[2]
Orbital Cortex	Orbital area 13a		Monkey[2]		Monkey[2]
Orbital Cortex	Orbital cortex				Rat[6]
Orbital Cortex	Ventral orbital cortex				Rat[7]
Orbital Cortex	Ventrolateral orbital cortex				Rat[7]
Pons	Caudal pontine reticular nuclei	Rabbit[3]	Rabbit[3]	Rabbit[3]	Rabbit[3]
Pons	Pontine reticular formation	Rabbit[3]	Rabbit[3]	Rabbit[3]	Rabbit[3]
Pons	Raphe magnus				Rabbit[3]
Prefrontal Cortex	Arcuate frontal eye field	Monkey[14]	Monkey[14]	Monkey[14]	Monkey[14]
Reticular Formation	Cuneiform nucleus			Rat[10]	
Reticular Formation	Reticular formation	Cat[1]	Cat[1]	Monkey[24]	Cat[1]
Spinal Cord	Dorsal horn				Rabbit[3]
Spinal Cord	Spinal cord	Cat[25]	Cat[25]	Cat[25]	Cat[25]
Superior Colliculus	Medial superior colliculus	Mouse[29]	Mouse[29]		
Superior Colliculus	Superior colliculus	Cat[26], Monkey[27]	Cat[26], Monkey[27]	Cat[26], Monkey[27]	Monkey[27,28]
Thalamus	Parafascicular nucleus				Rabbit [1]
Thalamus	Sub-thalamic nucleus		Monkey[30]		Rabbit [1]
Thalamus	Supragenicular nucleus	Rabbit[1]	Rabbit[1]	Rabbit[1]	Rabbit[1]
Zona Incerta	Zona incerta	Rabbit[1]	Rabbit[1]	Rabbit[1]	Rabbit[1], Rat[6]

PAG Efferent Connections					
Region	**Sub-region**	**DM**	**DL**	**L**	**VL**
Amygdala	Amygdala				Rabbit[31]
Amygdala	Central extended amygdala			Rat[32]	Rat[32]
Amygdala	Central nucleus of amygdala		Rat[4]	Rat[4]	Rat[4]
Basal Forebrain	Substantia innominata				Rabbit[31]
Brainstem	Nucleus incertus				Rat[33]
Brainstem	Subcoeruleus nucleus		Rat[34]		
Hippocampus	Hippocampus	*Not present*			
Hypothalamus	Posterior hypothalamic area			Rat[35]	Rat[35]
Hypothalamus	Ventrobasal hypothalamus	Rat[36]		Rat[36]	Rat[36]
Inferior Colliculus	Inferior colliculus			Rabbit[31]	Rabbit[31]
Locus Coeruleus	Locus coeruleus	Monkey[37]	Monkey[37], Rat[34]	Monkey[37], Rat[38]	Monkey[37], Rabbit [31], Rat[38,39]
Medulla Oblongata	Caudal ventrolateral medulla				Rat[40]
Medulla Oblongata	Lateral medulla			Monkey[41]	Monkey[41]
Medulla Oblongata	Lateral paragigantocellularis nucleus				Rat[34]
Medulla Oblongata	Nucleus raphe magnus	Cat[42], Monkey[37]	Monkey[37]	Cat[42], Monkey[37]	Cat[42], Monkey[37], Rat[34]
Medulla Oblongata	Paragigantocellularis nucleus		Rat[34]		Monkey[37]
Medulla Oblongata	Rostral ventral medulla				Rat[43]
Medulla Oblongata	Rostral ventrolateral medulla	Cat[44], Rat[45]		Cat[44]	Cat[44], Rat[45]
Medulla Oblongata	Rostro-ventromedial medulla	Rat[36]		Rat[36]	Rat[36]
Medulla Oblongata	Solitary nucleus		Rat[34]		Rat[34]
Medulla Oblongata	Spinal trigeminal nucleus				Monkey[37]
Medulla Oblongata	Trigeminal sensory complex	Rat[46]	Rat[46]	Rat[46]	Rat[46]
Pons	Lateral parabrachial nucleus	Rat[47]		Rat[47]	Rat[47]
Pons	Medial parabrachial nucleus	Rat[47]		Rat[47]	Rat[47]
Pons	Parabrachial nucleus	Rat[47]	Rat[47]	Rat[47]	Rat[47]
Pons	Reticulotegmental nucleus				Rabbit[31]
Pons	Ventrolateral pons	Monkey[48]	Monkey[48]	Monkey[48]	Monkey[48]
Reticular Formation	Caudal ventrolateral reticular nucleus				Rat[34]
Reticular Formation	Gigantocellular reticular nucleus		Rat[34]		
Reticular Formation	Nucleus ambiguus		Rat[34]	Monkey[4937]	Rat[34]
Reticular Formation	Nucleus cuneiformis	Monkey[37], Rabbit[31]	Monkey[37], Rabbit[31]	Rabbit[31]	Monkey[37], Rabbit[31]
Reticular Formation	Reticularis magnocellularis	Cat[42]		Cat[42]	Cat[42], Monkey[37]
Reticular Formation	Reticularis pontis oralis	Monkey[37]	Monkey[37]	Monkey[37]	Monkey[37]
Reticular Formation	Retroambiguus nucleus			Monkey[4150]	Monkey[50]
Reticular Formation	Rostral ventrolateral reticular nucleus				Rat[34]
Spinal Cord	Spinal cord			Monkey[51]	Monkey[51]
Substantia Nigra	Substantia nigra				Rat[43]
Superior Colliculus	Superior colliculus	Rabbit[31]	Rabbit[31]		Rabbit[31], Rat[39]

Thalamus	Caudal paraventricular nucleus	Rat[52]	Rat[52]	Rat[52]	Rat[52]
Thalamus	Central lateral thalamic nucleus	Rat[53]	Rat[53]	Rat[53]	Rat[53]
Thalamus	Central medial thalamic nucleus	Rat[53]		Rat[53]	Rat[53]
Thalamus	Intermediate paraventricular nucleus	Rat[52]	Rat[52]	Rat[52]	Rat[52]
Thalamus	Lateral parafascicular thalamic nucleus	Rat[53]		Rat[53]	
Thalamus	Medial parafascicular thalamic nucleus			Rat[53]	Rat[53]
Thalamus	Medial thalamus	Rat[36]		Rat[36]	Rat[36]
Thalamus	Mediodorsal thalamic nucleus		Rat[53]	Rat[53]	Rat[53]
Thalamus	Paracentral thalamic nucleus		Rat[53]	Rat[53]	Rat[53]
Thalamus	Parafascicular thalamic nucleus				Rat[39]
Thalamus	Paratenial thalamic nucleus			Rat[53]	
Thalamus	Rostral paraventricular nucleus	Rat[52]	Rat[52]	Rat[52]	Rat[52]
Thalamus	Sub-thalamic nucleus				Rabbit[31]
Thalamus	Submedius thalamic nucleus	Rat[53]	Rat[53]	Rat[53]	Rat[53]
Thalamus	Subparafasicular thalamic nucleus		Rat[53]		
Thalamus	Suprageniculate nucleus of the posterior thalamus				Rabbit[31]
Thalamus	Ventromedial thalamic nucleus			Rat[53]	Rat[53]
Ventral Midline of the Thalamus	Reuniens thalamic nucleus		Rat[53]	Rat[53]	Rat[53]
Ventral Midline of the Thalamus	Rhomboid thalamic nucleus			Rat	Rat[53]
Ventral Tegmental Area	Ventral tegmental area			Mouse[54]	Mouse[54], Rat[43]
Zona Incerta	Zona incerta	Rat[53]	Rat[53]	Rat[53]	Rat[39]

Table S1. Monosynaptic afferent and efferent connections of the PAG. Species in which connections were observed are listed in cells, with relevant citaitons listed below. Blank cells denotes the *absence of evidence* for or against a connection, to the best of our knowledge. Cells labeled "not present" in gray text denotes a study finding *evidence of absence.* The PAG receives afferent and efferent connections from both cortical and subcortical areas of the brain. Projections arising from cortical regions include the prefrontal cortex (An et al., 1998; Floyd et al., 2000; Hardy & Leichnetz, 1981), insular cortex (Benarroch, 2012; Neafsey et al., 1986), and the motor cortex (Beitz, 1982; Linnman et al., 2012; Mantyh, 1983a). Projections arising from subcortical and hindbrain areas, include the hypothalamus (Behbehani et al., 1988), amygdala (Rizvi et al., 1991) brainstem (Beitz et al., 1986), and spinal cord (Behbehani, 1995). The PAG's efferent connections project to brain areas that directly modulate the motor, behavioral, and sympathetic responses that operate to meet the demands of the ascending sensory information. These brain areas include the thalamus (Krout & Loewy, 2000), midbrain (Meller & Dennis, 1991), and brainstem (Mantyh, 1983b).

Peripheral Physiological Measure	Condition	Mean Difference	*t*	df	*p*	95% Confidence Interval of the Difference
SCR amplitude	One-back	0.018	3.268	67	0.0009	0.007 – 0.029
	Three-back	0.068	6.570	67	$< 4.4e^{-09}$	0.047 – 0.089
IBI	One-back*	9.642	3.637	58	0.0006	4.335 – 14.948
	Three-back	-12.472	3.825	58	0.0002	-19.000 – -5.944
RR	One-back	0.898	4.750	46	$< 1.0e^{-05}$	0.517 – 1.278
	Three-back	1.944	9.067	46	$< 4.2e^{-12}$	1.512 – 2.375

Table S2. One sample t-statistics for participants with high-quality physiological data (see *Peripheral Physiological Recording & Quality Assessment*). Preprocessed ANS measures (see Methods) were compared to baseline (i.e., 25-second fixation period prior to each block) and participant averages were computed for the 1-back and 3-back task periods. All *a priori* predictions are tested with one-tailed t-tests, and one unexpected result (increase in IBI from baseline during the 1-back condition) was tested with a two-tailed t-test (marked by an asterisk *). Abbreviations: ANS: autonomic nervous system; IBI: interbeat interval; RR: respiration rate; SCR: skin conductance response.

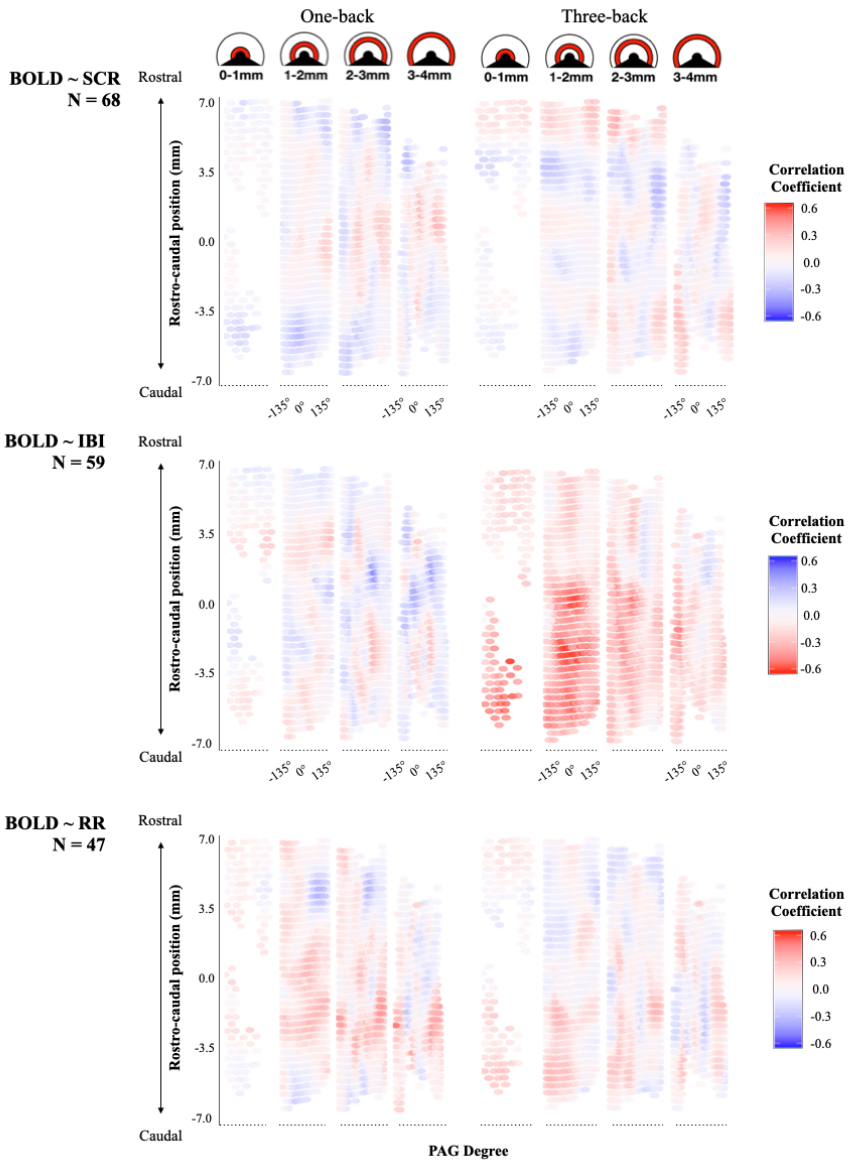

Figure S1. Cross-subject correlations between peripheral physiology voxelwise PAG BOLD signal intensity. Upper panels display radial cross-sections of the PAG cylinder (e.g., 0-1 mm). The y-axis illustrates voxel position along the rostral–caudal axis. The x-axis represents voxel position in degrees from the brain midline. The heat map illustrates magnitude (i.e., strength) of the correlation coefficients. Abbreviations: IBI: interbeat interval; RR: respiration rate; SCR: skin conductance response.

Supplemental References

1. Meller, S. T. & Dennis, B. J. Afferent projections to the periaqueductal gray in the rabbit. *Neuroscience* **19**, 927–964 (1986).
2. Hopkins, D. A. & Holstege, G. Amygdaloid projections to the mesencephalon, pons and medulla oblongata in the cat. *Exp. Brain Res.* **32**, 529–547 (1978).
3. An, X., Bandler, R., Ongür, D. & Price, J. L. Prefrontal cortical projections to longitudinal columns in the midbrain periaqueductal gray in macaque monkeys. *J. Comp. Neurol.* **401**, 455–479 (1998).
4. Rizvi, T. A., Ennis, M., Behbehani, M. M. & Shipley, M. T. Connections between the central nucleus of the amygdala and the midbrain periaqueductal gray: topography and reciprocity. *J. Comp. Neurol.* **303**, 121–131 (1991).
5. Frontera, J. L. *et al.* Bidirectional control of fear memories by cerebellar neurons projecting to the ventrolateral periaqueductal grey. *Nat. Commun.* **11**, 5207 (2020).
6. Mota-Ortiz, S. R., Sukikara, M. H., Felicio, L. F. & Canteras, N. S. Afferent Connections to the Rostrolateral Part of the Periaqueductal Gray: A Critical Region Influencing the Motivation Drive to Hunt and Forage. *Neural Plast.* **2009**, e612698 (2009).
7. Herrero, M. T., Insausti, R. & Gonzalo, L. M. Cortically projecting cells in the periaqueductal gray matter of the rat. A retrograde fluorescent tracer study. *Brain Res.* **543**, 201–212 (1991).
8. Floyd, N. S., Price, J. L., Ferry, A. T., Keay, K. A. & Bandler, R. Orbitomedial prefrontal cortical projections to distinct longitudinal columns of the periaqueductal gray in the rat. *J. Comp. Neurol.* **422**, 556–578 (2000).
9. Wyss, J. M. & Sripanidkulchai, K. The topography of the mesencephalic and pontine projections from the cingulate cortex of the rat. *Brain Res.* **293**, 1–15 (1984).
10. Beart, P. M., Summers, R. J., Stephenson, J. A., Cook, C. J. & Christie, M. J. Excitatory amino acid projections to the periaqueductal gray in the rat: A retrograde transport study utilizing d[3H]aspartate and [3H]GABA. *Neuroscience* **34**, 163–176 (1990).
11. Canteras, N. S. & Swanson, L. W. The dorsal premammillary nucleus: an unusual component of the mammillary body. *Proc. Natl. Acad. Sci.* **89**, 10089–10093 (1992).
12. Vertes, R. P. & Crane, A. M. Descending projections of the posterior nucleus of the hypothalamus: Phaseolus vulgaris leucoagglutinin analysis in the rat. *J. Comp. Neurol.* **374**, 607–631 (1996).
13. de Git, K. C. G. *et al.* Anatomical projections of the dorsomedial hypothalamus to the periaqueductal grey and their role in thermoregulation: a cautionary note. *Physiol. Rep.* **6**, e13807 (2018).
14. Bowden, D. M., German, D. C. & Douglas Poynter, W. An autoradiographic, semistereotaxic mapping of major projections from locus coeruleus and adjacent nuclei in Macaca mulatta. *Brain Res.* **145**, 257–276 (1978).
15. Shook, B. L., Schlag-Rey, M. & Schlag, J. Primate supplementary eye field: I. Comparative aspects of mesencephalic and pontine connections. *J. Comp. Neurol.* **301**, 618–642 (1990).
16. Powell, E. W. Septohabenular connections in the rat, cat and monkey. *J. Comp. Neurol.* **134**, 145–150 (1968).

17. Hardy, S. G. P. & Leichnetz, G. R. Cortical projections to the periaqueductal gray in the monkey: A retrograde and orthograde horseradish peroxidase study. *Neurosci. Lett.* **22**, 97–101 (1981).
18. Chiba, T., Kayahara, T. & Nakano, K. Efferent projections of infralimbic and prelimbic areas of the medial prefrontal cortex in the Japanese monkey, Macaca fuscata. *Brain Res.* **888**, 83–101 (2001).
19. Freedman, L. J., Insel, T. R. & Smith, Y. Subcortical projections of area 25 (subgenual cortex) of the macaque monkey. *J. Comp. Neurol.* **421**, 172–188 (2000).
20. Franklin, T. B. *et al.* Prefrontal cortical control of a brainstem social behavior circuit. *Nat. Neurosci.* **20**, 260–270 (2017).
21. Leichnetz, G. R. & Astruc, J. The efferent projections of the medial prefrontal cortex in the squirrel monkey (Saimiri sciureus). *Brain Res.* **109**, 455–472 (1976).
22. Sesack, S. R., Deutch, A. Y., Roth, R. H. & Bunney, B. S. Topographical organization of the efferent projections of the medial prefrontal cortex in the rat: An anterograde tract-tracing study with Phaseolus vulgaris leucoagglutinin. *J. Comp. Neurol.* **290**, 213–242 (1989).
23. Rinaman, L. Ascending projections from the caudal visceral nucleus of the solitary tract to brain regions involved in food intake and energy expenditure. *Brain Res.* **1350**, 18–34 (2010).
24. Bohlen, M. O., Warren, S. & May, P. J. A central mesencephalic reticular formation projection to the supraoculomotor area in macaque monkeys. *Brain Struct. Funct.* **221**, 2209–2229 (2016).
25. Björkeland, M. & Boivie, J. The termination of spinomesencephalic fibers in cat. *Anat. Embryol. (Berl.)* **170**, 265–277 (1984).
26. Evans, D. A. *et al.* A synaptic threshold mechanism for computing escape decisions. *Nature* **558**, 590–594 (2018).
27. Graham, J. An autoradiographic study of the efferent connections of the superior colliculus in the cat. *J. Comp. Neurol.* **173**, 629–654 (1977).
28. Mantyh, P. W. The ascending input to the midbrain periaqueductal gray of the primate. *J. Comp. Neurol.* **211**, 50–64 (1982).
29. May, P. J., Bohlen, M. O., Perkins, E., Wang, N. & Warren, S. Superior colliculus projections to target populations in the supraoculomotor area of the macaque monkey. *Vis. Neurosci.* **38**, (2021).
30. Smith, Y., Hazrati, L.-N. & Parent, A. Efferent projections of the subthalamic nucleus in the squirrel monkey as studied by the PHA-L anterograde tracing method. *J. Comp. Neurol.* **294**, 306–323 (1990).
31. Meller, S. T. & Dennis, B. J. Efferent projections of the periaqueductal gray in the rabbit. *Neuroscience* **40**, 191–216 (1991).
32. Hasue, R. H. & Shammah-Lagnado, S. J. Origin of the dopaminergic innervation of the central extended amygdala and accumbens shell: A combined retrograde tracing and immunohistochemical study in the rat. *J. Comp. Neurol.* **454**, 15–33 (2002).
33. Goto, M., Swanson, L. W. & Canteras, N. S. Connections of the nucleus incertus. *J. Comp. Neurol.* **438**, 86–122 (2001).
34. Cameron, A., Khan, I., Westlund, K. & Willis, W. The efferent projections of the periaqueductal gray in the rat: A Phaseolus vulgaris-leucoagglutinin study. II. Descending projections. *J. Comp. Neurol.* (1995) doi:10.1002/CNE.903510408.

35. Abrahamson, E. E. & Moore, R. Y. The posterior hypothalamic area: chemoarchitecture and afferent connections. *Brain Res.* **889**, 1–22 (2001).
36. Reichling, D. B. & Basbaum, A. I. Collateralization of periaqueductal gray neurons to forebrain or diencephalon and to the medullary nucleus raphe magnus in the rat. *Neuroscience* **42**, 183–200 (1991).
37. Mantyh, P. W. Connections of midbrain periaqueductal gray in the monkey. II. Descending efferent projections. *J. Neurophysiol.* **49**, 582–594 (1983).
38. Ennis, M., Behbehani, M., Shipley, M. T., van Bockstaele, E. J. & Aston-Jones, G. Projections from the periaqueductal gray to the rostromedial pericoerulear region and nucleus locus coeruleus: Anatomic and physiologic studies. *J. Comp. Neurol.* **306**, 480–494 (1991).
39. Mihaly, E., Legradi, G., Fekete, C. & Lechan, R. M. Efferent projections of ProTRH neurons in the ventrolateral periaqueductal gray. *Brain Res.* **919**, 185–197 (2001).
40. Henderson, L. A., Keay, K. A. & Bandler, R. The ventrolateral periaqueductal gray projects to caudal brainstem depressor regions: a functional-anatomical and physiological study. *Neuroscience* **82**, 201–221 (1998).
41. Vanderhorst, V. G. J. M., Terasawa, E. & Ralston, H. J. Projections from estrogen receptor-α immunoreactive neurons in the periaqueductal gray to the lateral medulla oblongata in the rhesus monkey. *Neuroscience* **125**, 243–253 (2004).
42. Abols, I. A. & Basbaum, A. I. Afferent connections of the rostral medulla of the cat: A neural substrate for midbrain-medullary interactions in the modulation of pain. *J. Comp. Neurol.* **201**, 285–297 (1981).
43. Suckow, S. K., Deichsel, E. L., Ingram, S. L., Morgan, M. M. & Aicher, S. A. Columnar Distribution of Catecholaminergic Neurons in the Ventrolateral Periaqueductal Gray (vlPAG) and Their Relationship to Efferent Pathways. *Synap. N. Y. N* **67**, 94–108 (2013).
44. Carrive, P. & Bandler, R. Control of extracranial and hindlimb blood flow by the midbrain periaqueductal grey of the cat. *Exp. Brain Res.* **84**, 599–606 (1991).
45. Bowman, B. R., Kumar, N. N., Hassan, S. F., McMullan, S. & Goodchild, A. K. Brain sources of inhibitory input to the rat rostral ventrolateral medulla. *J. Comp. Neurol.* **521**, 213–232 (2013).
46. Li, Y.-Q., Takada, M., Shinonaga, Y. & Mizuno, N. Direct projections from the midbrain periaqueductal gray and the dorsal raphe nucleus to the trigeminal sensory complex in the rat. *Neuroscience* **54**, 431–443 (1993).
47. Krout, K. E., Jansen, A. S. P. & Loewy, A. D. Periaqueductal gray matter projection to the parabrachial nucleus in rat. *J. Comp. Neurol.* **401**, 437–454 (1998).
48. Hannig, S. & Jürgens, U. Projections of the ventrolateral pontine vocalization area in the squirrel monkey. *Exp. Brain Res.* **169**, 92–105 (2006).
49. Jürgens, U. & Pratt, R. Role of the periaqueductal grey in vocal expression of emotion. *Brain Res.* **167**, 367–378 (1979).
50. Vanderhorst, V. G. J. M., Terasawa, E., Ralston III, H. J. & Holstege, G. Monosynaptic projections from the lateral periaqueductal gray to the nucleus retroambiguus in the rhesus monkey: Implications for vocalization and reproductive behavior. *J. Comp. Neurol.* **424**, 251–268 (2000).
51. Castiglioi, A. J., Gallaway, M. C. & Coulter, J. D. Spinal projections from the midbrain in monkey. *J. Comp. Neurol.* **178**, 329–345 (1978).

52. Boorman, D. C., Brown, R. & Keay, K. A. Periaqueductal gray inputs to the paraventricular nucleus of the thalamus: Columnar topography and glucocorticoid (in)sensitivity. *Brain Res.* **1750**, 147171 (2021).
53. Krout, K. E. & Loewy, A. D. Periaqueductal gray matter projections to midline and intralaminar thalamic nuclei of the rat. *J. Comp. Neurol.* **424**, 111–141 (2000).
54. Ntamati, N. R., Creed, M., Achargui, R. & Lüscher, C. Periaqueductal efferents to dopamine and GABA neurons of the VTA. *PLOS ONE* **13**, e0190297 (2018).